TITLE:

Structural analysis of cholesterol binding and sterol selectivity by ABCG5/G8.

AUTHOR NAMES:

Danny Farhat[1,‡], Fatemeh Rezaei[1,‡], Milica Ristovski[1,2,‡!], Yidai Yang[1], Albert Stancescu[1,3,#], Lucia Dzimkova[1,4], Sabrina Samnani[1,4], Jean-François Couture[1] and Jyh-Yeuan Lee[1,*]

AUTHOR ADDRESSES:

[1] Department of Biochemistry, Microbiology and Immunology, Faculty of Medicine, University of Ottawa, Ottawa, Ontario, Canada

[2] Translational and Molecular Medicine Program, Faculty of Medicine, University of Ottawa, Ontario, Ottawa, Canada

[3] Biochemistry Program, Faculty of Health Sciences, McMaster University, Hamilton, Ontario, Canada

[4] Biochemistry Program, Faculty of Science, University of Ottawa, Ottawa, Ontario, Canada

KEYWORDS:

ABCG5, ABCG8, ABCG sterol transporters, cholesterol, sterol selectivity, X-ray crystallography, molecular docking

AUTHOR INFORMATION

* Correspondence should be addressed to Jyh-Yeuan (Eric) Lee (Jyh-Yeuan.Lee@uOttawa.ca).

‡ Contributed equally.

Current address: MBiotech Program, University of Toronto-Mississauga

! Current address: Undergraduate Medical Education, Faculty of Medicine, University of Ottawa

ABSTRACT:

The ATP-binding cassette (ABC) sterol transporters are responsible for maintaining cholesterol homeostasis in mammals by participating in reverse cholesterol transport (RCT) or transintestinal cholesterol efflux (TICE). The heterodimeric ABCG5/G8 carries out selective sterol excretion, preventing the abnormal accumulation of plant sterols in human bodies, while homodimeric ABCG1 contributes to the biogenesis and metabolism of high-density lipoproteins. A sterol-binding site on ABCG5/G8 was proposed at the interface of the transmembrane domain and the core of lipid bilayers. In this study, we have determined the crystal structure of ABCG5/G8 in a cholesterol-bound state and developed an *in vitro* assay to characterize its cholesterol-binding activity. The structure combined with amino acid sequence analysis shows that in the proximity of the sterol-binding site, a highly conserved phenylalanine array is critical for ABCG cholesterol/sterol transporter functions. Lastly, *in silico* docking analysis of cholesterol and stigmasterol (a plant sterol) suggests sterol-binding selectivity on ABCG5/G8, but not ABCG1. Together, our results provide a structural basis for cholesterol binding on ABCG5/G8 and the sterol selectivity by ABCG transporters.

1. INTRODUCTION

Lipid homeostasis in mammalian cells is a critical process regulated in part by the ATP binding cassette (ABC) lipid transporters, particularly the ABCG and ABCA cholesterol transporters, such as ABCG1, ABCG4, ABCG5/G8 and ABCA1. As a critical component of cellular membranes, cholesterol comprises >50% of total cellular lipid content and is further utilized as the precursor molecule for steroid hormones that modulate gene regulation as well as bile acids that are required for nutrient absorption. To maintain cholesterol balance, excess cholesterol must be eliminated from cells and tissues via the reverse cholesterol transport (RCT) pathway by circulating high-density lipoproteins (Nan et al., 2004; Vaughan and Oram, 2005; Yu et al., 2005). Within the human ABCG protein subfamily, all members function as lipid floppases, with the notable exception of ABCG2, that opts for a more relaxed approach to substrate efflux by working as the sole multidrug transporter (MDR) of the subfamily (Allen et al., 2002; Austin et al., 1998). In addition, the PDR subfamily of full-length transporters (ABCG2 homologues in *Saccharomyces cerevisiae*) are related to ABCG and sharing the structural fold and inverted topology (Mahé et al., 1996). Moreover, ABCG transporters are becoming increasingly important with new findings uncovering their physiological roles in severe chronic diseases, notably such as cancer, atherosclerosis, diabetes and Alzheimer's disease (Berge et al., 2000; Do et al., 2012; Lee et al., 2001; Meurs et al., 2012; Namba et al., 2018; Tian et al., 2017). While these proteins have gained more notoriety, the efflux mechanisms have remained a mystery, with various proposed hypotheses that are yet to be agreed upon.

In mammals, ABCG lipid transporters consist of the heterodimeric ABCG5/G8 and the homodimeric ABCG1 or ABCG4 complexes. ABCG5/G8 is localized on the canalicular membranes of the bile ducts in the liver and the brush border of enterocytes in the small intestines,

where it mediates the final step of the RCT (Berge et al., 2000; Liqing et al., 2002; Patel et al., 1998; Zein et al., 2019). ABCG1 and ABCG4 translocate cholesterol within the plasma membrane and in endosomes (Pandzic et al., 2017; Sano et al., 2014) and play a key role in the regulating cholesterol balance in the lung, the brain and in macrophage-rich tissues (Bojanic et al., 2010; de Aguiar Vallim et al., 2017; Sag et al., 2015; Savary et al., 1996). ABCG5/G8 undergoes obligatory heterodimerization and is unique in its capability of preferential efflux for dietary plant sterols over cholesterol (Berge et al., 2000; Graf et al., 2003; Lee et al., 2001; Yang et al., 2004). The mechanisms that govern such substrate selectivity within this protein subfamily, however, remains elusive. Based on the crystal structure of ABCG5/G8, we can now theorize that such substrate specificity among ABCG transporters may be the result of the difference in hydrophobic valve composition between the multidrug transporter: ABCG2 and the lipid transporters: ABCG1, ABCG4, ABCG5/G8 (Khunweeraphong et al., 2020, 2019). In addition, a sterol-binding site was postulated at the membrane-transporter interface based on the crystal structure of ABCG5/G8 (Lee et al., 2016), whereas studies in recent ABCG1 structures (Skarda et al., 2021; Sun et al., 2021) have suggested sterol binding at the cytoplasmic end of the transmembrane domain (TMD).

The general TMD topology is shared among ABCG subfamily proteins. Each half transporter consists of six transmembrane helices (TMH) and the re-entry helices that are part of the extracellular domains. A connecting helix bridges the TMD to the nucleotide-binding domain (NBD), forming an amphipathic interface on the cytoplasmic leaflet of the lipid bilayers. Meanwhile a triple-helical bundle brings the TMDs and the NBDs together to create a compact and short-stacked transporter conformation (Khunweeraphong et al., 2020; Lee et al., 2016). At the cellular level, ABC lipid transporters have been shown to alter the composition of their local membrane environment. Such revisions may come from the subduing of lipid rafts by

redistributing the high cholesterol content towards the surrounding membrane regions (Ristovski et al., 2021; Sano et al., 2014). Using *in vivo* and *in vitro* functional assays, we have previously characterized a loss-of-function (LOF) mutation $ABCG5_{A540F}$, a conserved residue near a putative sterol-binding site in ABCG5/G8 (Lee et al., 2016; Xavier et al., 2020). These findings suggested the likelihood of an access site that allows the binding of cholesterol binding prior to its re-localization within the membrane-embedded portion of the sterol transporters.

One of the significant challenges in studying the cholesterol-transporter interaction is to accurately identify the sterol molecules as either the transport substrates or the intrinsic component of cell membranes. The latter can also play regulatory roles in membrane protein functions, such as ABCG2 (Telbisz et al., 2013) or G-protein coupled receptors (Gimpl, 2016). Besides experimental approaches to obtain atomic models by crystallography or electron microscopy, *in silico* molecular docking can allow researchers to predict the ligand-binding sites on a protein by using available structural models and ligand libraries. The availability of specific ABCG5/G8 and ABCG1 structures can now provide the framework, allowing the necessary *in silico* tools to simulate snapshots of interactions between sterol ligands and the transporter proteins.

In this study, we first carried out amino acid sequence analysis of ABCG transporters, highlighting key conserved aromatic residues arranged in a spatially conserved pattern on TMH2. We solved the crystal structure of ABCG5/G8 in complex with cholesterol. The structure shows that an orthogonal cholesterol molecule fitting horizontally in front of A540, a conserved ABCG5 residue at this orthogonal sterol-binding site. In parallel, optimization of an *in vitro* cholesterol-binding assay showed the sterol binding activities of both WT ABCG5/G8 and mutant $ABCG5_{A540F}$/G8. To determine the differential sterol binding activities on ABCG sterol transporters, blind molecular docking analysis was conducted on wild-type (WT) ABCG5/G8 or

ABCG1 in the presence of cholesterol or stigmasterol, as well as selective mutants $ABCG5_{Y432F}$, $ABCG8_{N564P}$ and $ABCG5_{A540F}$. We also analyzed the cholesterol-binding patterns on the ATP bound states by using both experimental and homology models, showing the sterols only accumulated on the surface of the extracellular domain, likely a terminal state during the ATP-coupled sterol-transport cycle. Together with previous *in vivo* and *in vitro* observations, our results provide a structural basis for sterol selectivity of ABCG lipid transporters and a visual component to the sterol-transport mechanism.

2. RESULTS

2.1 Conserved phenylalanine cluster on THM2 of ABCG transporters:

Recent structural determination of ABCG transporters by cryo-electron microscopy (Skarda et al., 2021; Sun et al., 2021; Xu et al., 2022; Zhang et al., 2021) confirms the general molecular architecture as initially revealed by the crystal structure of an apo ABCG5/G8 (Lee et al., 2016). The TMH2 and TMH5 of both subunits are adjacent to one another, forming a dimer interface within the transmembrane domains. This interface has been hypothesized to be a sterol translocation pathway based on sterol localization as observed in the EM structures. However, to what extent this pathway contributes to sterol translocation remains unclear. In this study, we used multiple sequence alignment to analyze the amino acid sequence conservation in the TMH2 of human ABCG1/2/4/5/8, PDR5 of the yeast *Saccharomyces cerevisiae* (Harris et al., 2021), and White protein of *Drosophila melanogaster* (Ferreiro et al., 2018; Mahé et al., 1996)(**Fig. 1**). Among these seven ABCG transporters, White is a close homologue to ABCG1, while the drug resistant PDR5 is an ABC drug transporter and an ABCG2 homologue. Using ABCG1 as sequence reference and analyzing 250-300 mammalian orthologs, each ABCG member includes a highly conserved phenylalanine (or tyrosine in ABCG5) at position F1 (**Fig 1A**). The adjacent position F2 shows similar conservation of hydrophobic residues, albeit with a more relaxed sequence homology than F1 (**Fig 1A**). Position F3 reveals a conserved phenylalanine in ABCG1, ABCG4 and the N-terminal half of PDR5 (PDR5-1), although the C-terminal half of PDR5 (PDR5-2) has a conserved phenylalanine just one residue off from F3. Position F4 shows the last highly conserved phenylalanine found on TMH2 (**Fig 1A**). These conserved phenylalanine residues are visualized through a Logo plot (**Fig 1B**), indicating at least two phenylalanine residues being flanked between positions F1 and F4 on the hydrophobic residue-rich TMH2.

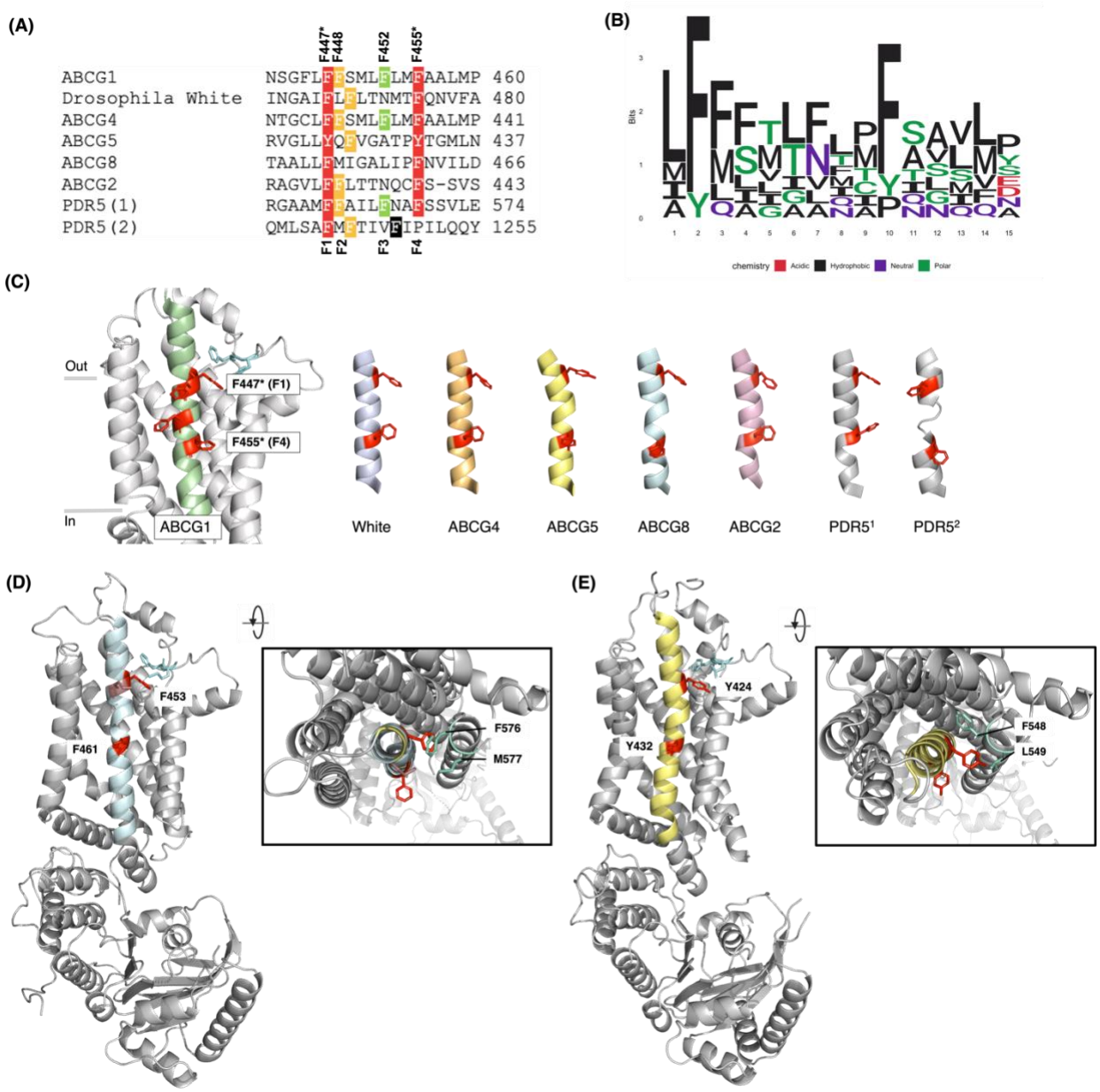

Figure 1. Conservation of aromatic amino acids on TMH2 of human ABCG family protein and homologues, including their localization in relation to key regions in the ABCG5/G8 heterodimer. (A) Sequence analysis of transmembrane helix five (TMH2) was done through PROMALS3D. Residues were screened for high conservation through BLAST sequence analysis. Red highlights perfect (or near perfect) aromatic residue conservation. Orange highlights conservation with ± 1 residue displacement. Green shows moderate conservation. Black shows non-sequence, but rather structural conservation. **(B)** Logo plot of TMH2 residues are colored according to their chemical nature. Red: acidic amino acids; Black: hydrophobic amino acids; Purple: neutral residues; Green: polar residues. **(C)** Structural conservation of highlighted aromatic amino acids from (A), using ABCG1 amino acid numeration as a reference. ABCG1 (PDB ID:

7OZ1, green), ABCG2 (PDB ID: 6VXI, pink , ABCG5/G8 (PDB ID: 5DO7; G5 in blue, G8 in yellow), PDR5-1 and 2 (PDB ID: 7PO3, light grey). *Drosophila* White (purple) and ABCG4 (orange) are the only two Alphafold models, both have helices with predicted local distance difference test score of >90. F447 (F1) and F455 (F4) residues in relation to ABCG1, have the highest conservation. The residues directions are maintained, with F447 stacking under the hydrophobic valve and F455 pointing towards the lumenal space between the TMD dimer. ABCG5 is the only monomer which has tyrosine's instead of phenylalanine's. ABCG1 and ABCG4 have large hydrophobic amino acids pointing lumenally causing a mass hydrophobic region spanning most of the transmembrane domain. **(D, E)** ABCG5/G8 heterodimer is split and shown in a top-down view, highlighting the location of conserved F453 and Y424 in relation to hydrophobic valves. **(D)** In ABCG8, F453 (F1) stacks underneath F576, which (along M577) comprise the hydrophobic valve shown in blue. **(E)** In ABCG5, Y424 (F1) is stacked underneath both hydrophobic valve residues; F548 and L549, shown in blue.

When inspecting the spatial relationship of these phenylalanine residues, we observed an open space immediately below the hydrophobic valve and above a cavity that is open to the cytoplasm in the inward-facing conformation of ABCG transporters (**Fig. 1C, left**). Not only are the F1-4 residues shared among the eight homologous monomers, but two or three aromatic side chains also point inwards the TMD dimer interface, creating a highway-shaped open space (**Fig 1C, right**). We have coined this open space as the Phenylalanine Highway (PH) to highlight this unique structural motif in the transmembrane domain. ABCG1 and ABCG4 share the most closely spaced phenylalanine residues in their iteration of the PH, while the F2 in White is one residue off from that in ABCG1. ABCG2, ABCG8 and PDR5 (either the N- or C-terminal half) have similar spacing of their phenylalanine residues, whereas the equivalent residues on ABCG5 are replaced by aromatic tyrosine residues. In addition, the phenylalanine side chains may be adjusted based on the ligand placements (**Suppl Fig. 1**). Moreover, position F1 is spatially adjacent to the aromatic residues of the previously described hydrophobic valve (or ABCG2's di-leucine valve/gate), forming a closed interface in the inward-facing protein conformation (**Fig 1D & 1E**) (Khunweeraphong et al., 2020). Speculatively, when the hydrophobic valve opens, the phenylalanine side chains may move away from the valve.

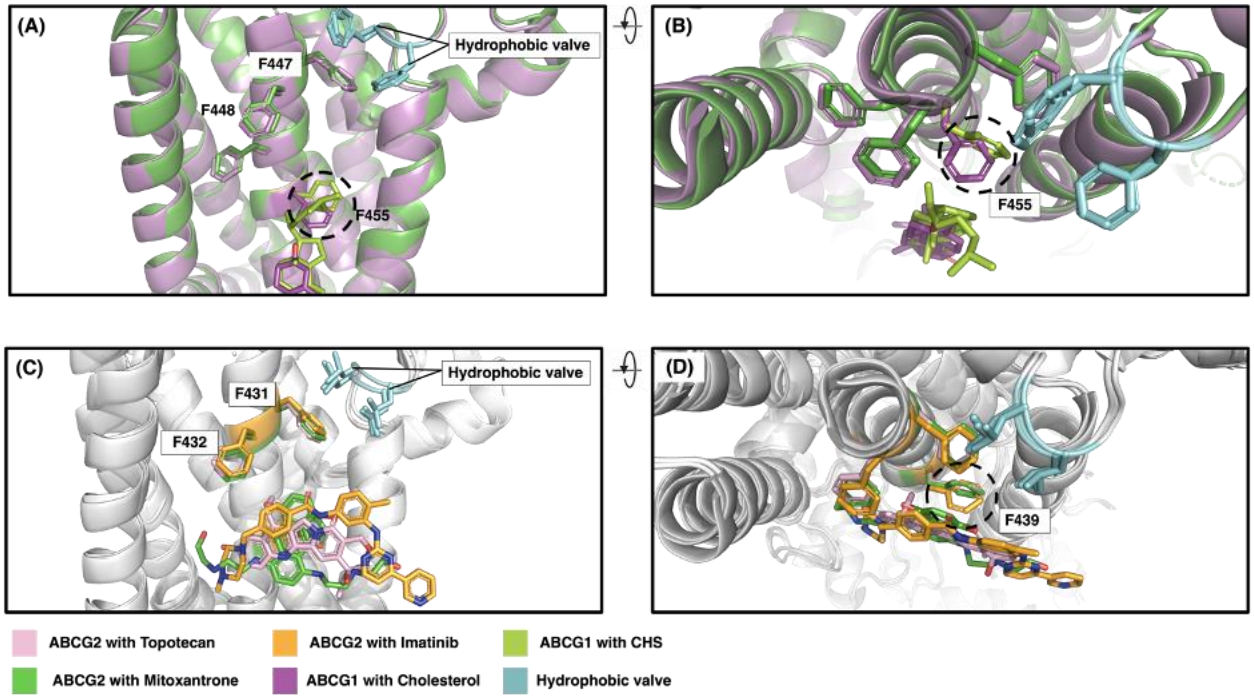

Supplementary Figure 1. Superposition of the phenylalanine highway on ABCG1 and ABCG2. (A). Side view of ABCG1, showing the difference in height of CHS (green) and cholesterol (pink). **(B)** Top-down view ABCG1 bound to CHS (PDB ID : 7OZ1, green) aligned with ABCG1 bound to cholesterol (7R8D, pink/red) emphasizing the difference in F455 rotation when interacting with different length ligands. Rotation occurs when longer ligands (such as CHS) reach deep enough into the transmembrane cavity, causing the alpha carbon and phenyl side chain of F455 to rotate. F447 is also seen stacked under hydrophobic valve. **(C)** Side view of ABCG2, showing the difference in localization of Imatinib (orange), Topotecan (pink), Mitoxantrone (green). **(D)**Top-down view of ABCG2 bound with Imatinib (PDB ID: 6VXH, orange), Topotecan (PDB ID :6VXJ, pink) and Mitoxantrone (PDB ID: 6VXI, green). Rotation of F439 is seen when substrates are deep enough into the cavity to interact with the residue. Contrarily, when they are not, such rotation events do not happen, as observed with Imatinib.

2.2 Crystal structure of ABCG5/G8 in an orthogonal cholesterol-binding state:

Several *bona fide* sterol molecules were observed on recent cryo-EM structures of ABCG1 or ABCG5/G8, which led to various models of their sterol-transport (or binding) mechanisms, but more structural data and further mechanistic analysis are still required to establish a convergent model of cholesterol transport. We have previously crystallized human ABCG5/G8 in an apo state by bicelle crystallization. To gain the structural basis of the sterol-transport (or binding)

mechanism, in this study, we determined a cytoplasmic-facing crystal structure of cholesterol-bound ABCG5/G8 at 4Å by X-ray crystallography. Three X-ray diffraction datasets were integrated and scaled with acceptable statistics. The initial model was obtained by molecular replacement using a previously resolved cryo-EM structure (PDB ID: 7JR7) (Zhang et al., 2021), and the motifs involved in ATP binding were adjusted based on the previous crystal structure (PDB ID: 5DO7) (Lee et al., 2016). Two ABCG5/G8 heterodimers are observed in the asymmetric unit. The protein model in this report includes a corrected amino acid registry in the nucleotide-binding domain as previously highlighted by Zhang *et al.* Additionally, it shows a consistent overall architecture and key structural features as described previously, overall root mean square deviation (RMSD) of ~0.9 Å when superimposed (Lee et al., 2016; Zein et al., 2019; Zhang et al., 2021)(**Fig. 2A**). After initial refinement, we observed two clear electron densities at the interface of symmetrically located transmembrane domains of these two transporters, which resembled the polycyclic characteristic of cholesterol molecules. Therefore, we added two cholesterol molecules to the initial model for further refinement and obtained a significant improvement of the Rfree from 0.338 to 0.302 and reasonable geometrical validation at current resolution. The final model shows an orthogonal cholesterol molecule in close contact with $ABCG5_{A540}$ (namely the ABCG5-dominant side), with the 3-β-hydroxyl group forming a weak hydrogen bonding with the side chain of $ABCG8_{T430}$ (4.3-4.5 Å). No sterol was observed on the equivalent side of ABCG8 (namely the ABCG8-dominant side) (**Fig. 2B**). Selected regions of the electron densities are shown in Suppl Fig. 2. The statistics of data processing and model refinement are summarized in **Table 1**.

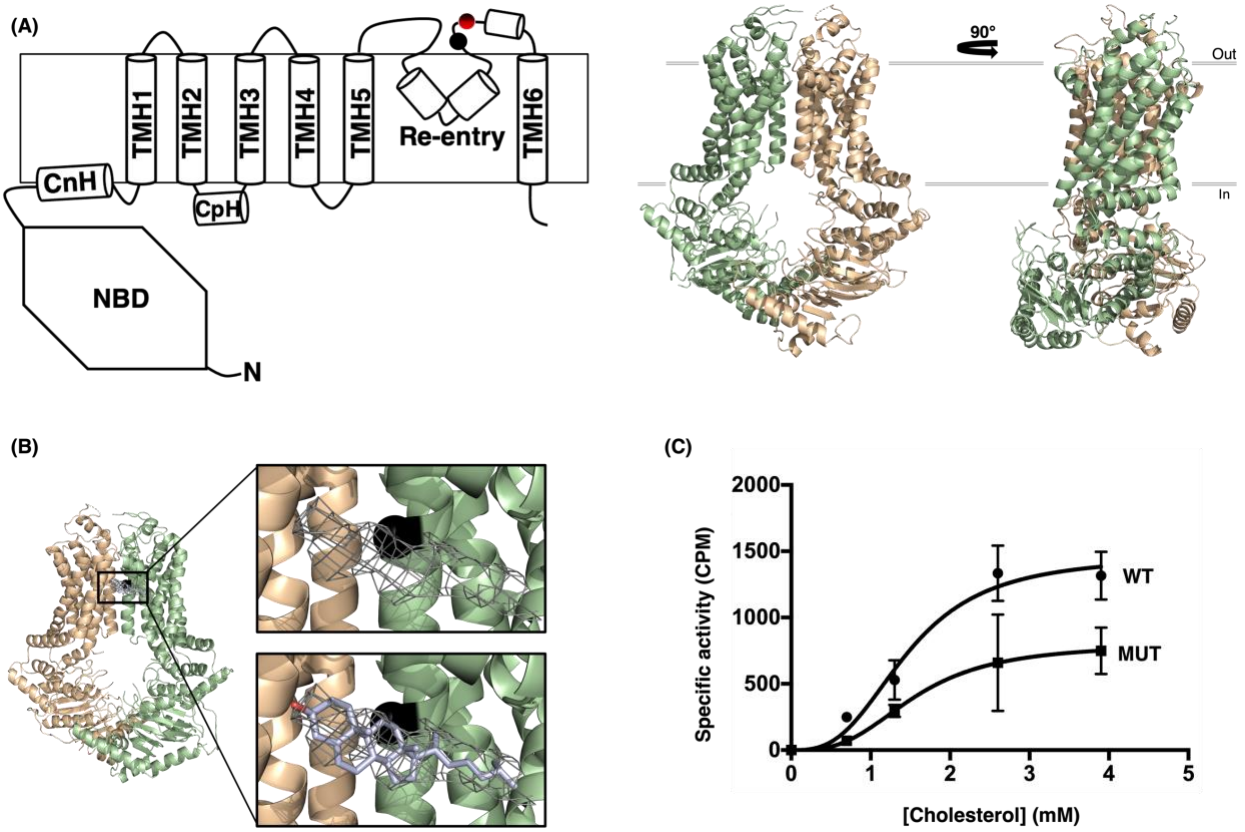

Figure 2. Crystal structure of cholesterol-bound ABCG5/G8 and cholesterol-binding assay. **(A)** *Left,* Topological representation of the ABCG5/G8 crystal structure is depicted in empty cylinders, showing the transmembrane structural segments of ABCG5/G8 including connecting helixes (CnH), TM helixes, coupling helices (CpH), and re-entry helixes. *Right,* The cartoon illustration of the ABCG5/G8 heterodimer with ABCG5 in wheat and ABCG8 in light-green colors. The N-glycosylation sites are shown in solid circles: $ABCG5_{N592}$ or $ABCG8_{N619}$ in red and black, $ABCG5_{N584}$ in black. **(B)** Cholesterol-bound ABCG5/G8 structure is plotted in cartoon presentation. The first zoomed-in picture shows the electron density related to the cholesterol molecule which was observed at the interface of transmembrane domains of the crystallographic dimers (top right). The cholesterol molecule was modeled to the primary structure as shown in the second zoomed-in picture (bottom right). Alanine 540 (A540) is marked in a black sphere as a residue involved in the cholesterol-binding site. **(C)** The cholesterol-binding activities of the WT and the A540F mutant were measured by using [^{3}H]-cholesterol, showing the binding parameters for the WT and the mutant with Bmax = 50.64±0.77 and 27.65±0.01 μCi/ml, K_D = 1.46 ±0.28 and 1.55±0.01 μM, and h = 2.91 and 2.98, respectively. A P-value = 0.043 was obtained by paired t-test between WT and mutant. All calculations were performed using GraphPad Prism programs.

With an *in vivo* analysis of biliary cholesterol secretion and an *in vitro* ATPase assay, we have previously characterized a loss-of-function (LOF) mutant $ABCG5_{A540F}$/G8 (A540F), predicting a putative sterol-binding at this transporter-membrane interface (Lee et al., 2016; Xavier et al., 2020). In this study, we developed an *in vitro* cholesterol-binding assay using tritiated cholesterol (see Materials and Methods) and characterized cholesterol binding on purified ABCG5/G8 WT and A540F mutant proteins (**Fig. 2C**). The reaction reached a saturation of cholesterol at ~3 μM, where the mutant showed about two-fold inhibition of the maximal cholesterol-binding rate. The binding constant K_D and Hill coefficient h were estimated as 1.46 ± 0.28 μM (h = 2.91) and 1.55 ± 0.01 μM (h = 2.98) for the WT and mutant proteins, respectively. Given the ATPase activity of A540F mutation was suppressed by ~90% with similar K_M for sterols (Xavier et al., 2020), both assays suggest a functionally defective conformation by this LOF mutant. Together with the new structural data, our analyses confirmed the role of the orthogonal cholesterol-binding site in proximity to $ABCG5_{A540}$ (**Fig. 2B**).

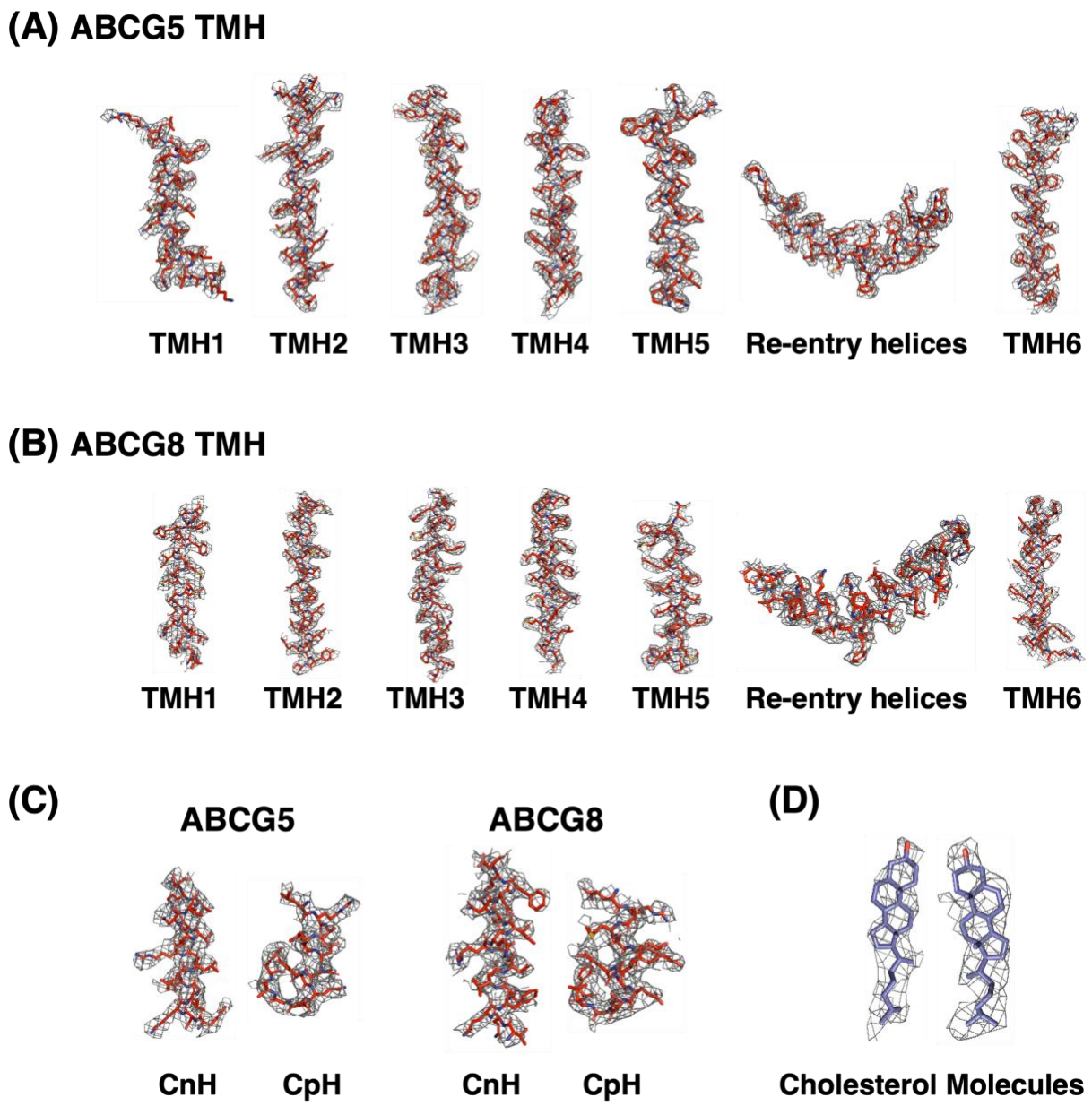

Supplementary Figure 2. The fitting of the structural model in the electron densities (2Fo-Fc omit map). The representative segments of the human ABCG5/G8 proteins, including transmembrane (A/B), connecting (C), coupling helixes (C), and cholesterol molecules (D) are shown separately for G5 and G8 chains in the electron density with a mesh contoured at 1 σ and the thickness of 1.5 as implemented in PyMOL.

2.3 Asymmetric binding of cholesterol or stigmasterol on ABCG5/G8, but not ABCG1:

The ABC transporter superfamily translocate a broad spectrum of substrates across cellular

membranes, with individual members conveying their unique substrate specificities. To determine how ABCG transporters bind sterol ligands, we used previously published apo models ABCG5/G8 (PDB ID: 5DO7 or 7JR7) and ABCG1 (PDB ID: 7R8D) (Lee et al., 2016; Zhang et al., 2021) and carried out molecular docking on the TMD with cholesterol or stigmasterol, a plant sterol previously shown to have the highest accumulation rate in an Abcg5/g8-deficient mouse model (Yu et al., 2004). Using UCSF DOCK6 suite (Allen et al., 2015), we first optimized the docking protocol by carrying out a redocking of the ligands (topotecan, mitoxantrone and imatinib) to reproduce their complex with ABCG2. Additional redocking was done on a distinct ABCG2 model to further evaluate docking optimization. (**Suppl Fig. 3**) (Jackson et al., 2018; Orlando and Liao, 2020).

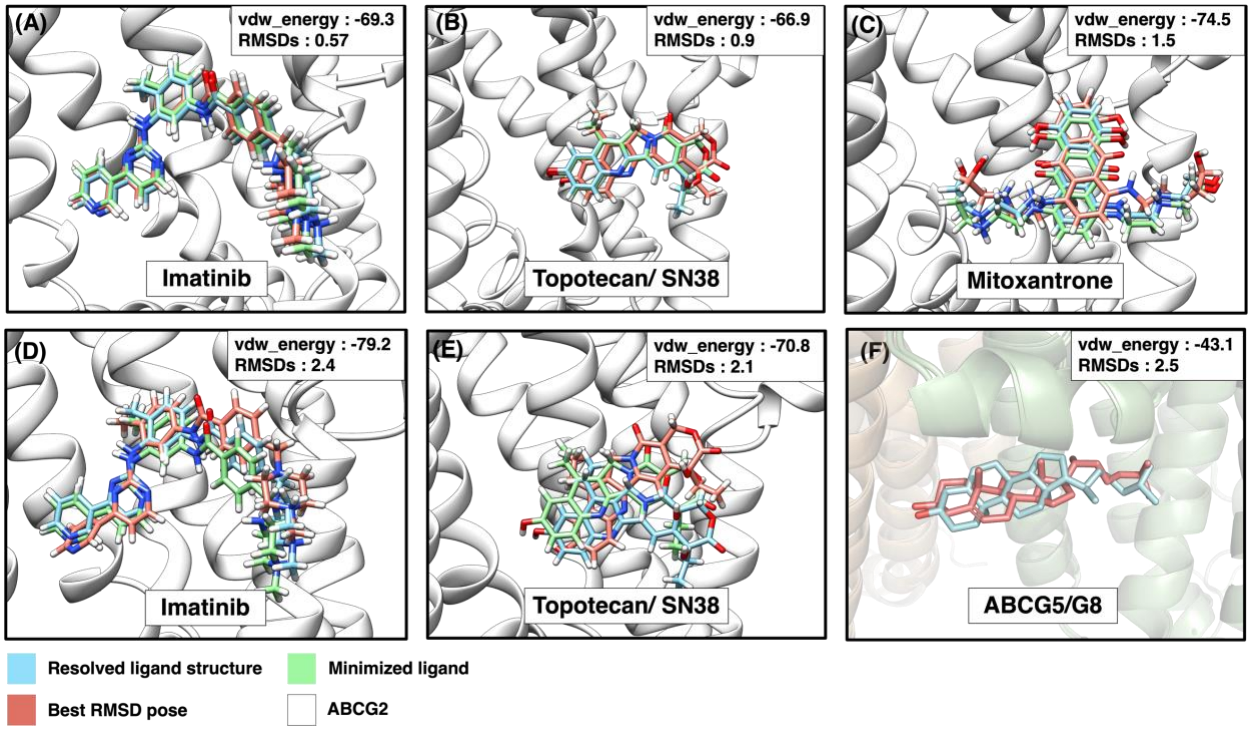

Supplementary Figure 3. Resolved ligand structures compared to dock prediction in ABCG2 (A-E) and ABCG5/G8 (F). (**A-C**) **Redocking of** resolved ligands on ABCG2 (blue): Topotecan/SN38 (PDB ID :6VXJ), Mitoxantrone (PDB ID: 6VXI), and Imatinib (PDB ID : 6VXH). Green highlights the minimized rigid conformation as calculated by Dock6.9. Orange

highlights the best predicted pose. Blue ligands were observed in the experimentally determined structures. RMSD of all superpositions is (0.57Å – 1.5Å). (**D/E**) Ligands were aligned and docked to ABCG2 (PDB ID: 6FFC). Pink highlights the best RMSD predicted pose. The RMSD of all superpositions is (2.1Å – 2.4Å). (**F**) Redocking of cholesterol ligand on ABCG5/G8 (2.5Å, present study). See details in Materials and Methods.

Figure 3 shows the docking results of all acceptable (or viable) poses for the two sterol ligands, cholesterol and stigmasterol, on the ABCG sterol transporters according to the standard flexible docking protocol as implemented in DOCK6 suites (Allen et al., 2015). On ABCG5/G8, poses of sterols are distributed asymmetrically at the opposing membrane-transporter interfaces, having more docking conformations on the ABCG5-dominant side (**Fig. 3A/B**). The predicted orthogonal cholesterol (*i.e.*, one of the top-3 poses) has a nearly identical position to the cholesterol molecule in the newly determined cholesterol-bound structure (**Fig. 2 & 3D/E**). On the ABCG8-dominant side, no orthogonal sterol was obtained, and either ligands are clustered on the inner leaflet of the membrane's lipid-bilayered and with the topmost sterols in close distance from the lower end of the PH (*i.e.*, $ABCG5_{Y432}$ or $ABCG1_{F455}$). Such asymmetric sterol binding on ABCG5/G8 suggests another level of functional asymmetry by ABCG5/G8-mediated sterol transport. On the ABCG1 homodimer, acceptable poses are only observed on the inner leaflet of the lipid-bilayered membranes, resembling those on the ABCG8-dominant side, and bound sterols can be equally distributed on either side of the transporter-membrane interface (**Fig. 3A/B, bottom**). Such symmetric sterol binding is distinct from ABCG5/G8, suggesting different mechanisms of using the PH between ABCG1 and ABCG5/G8.

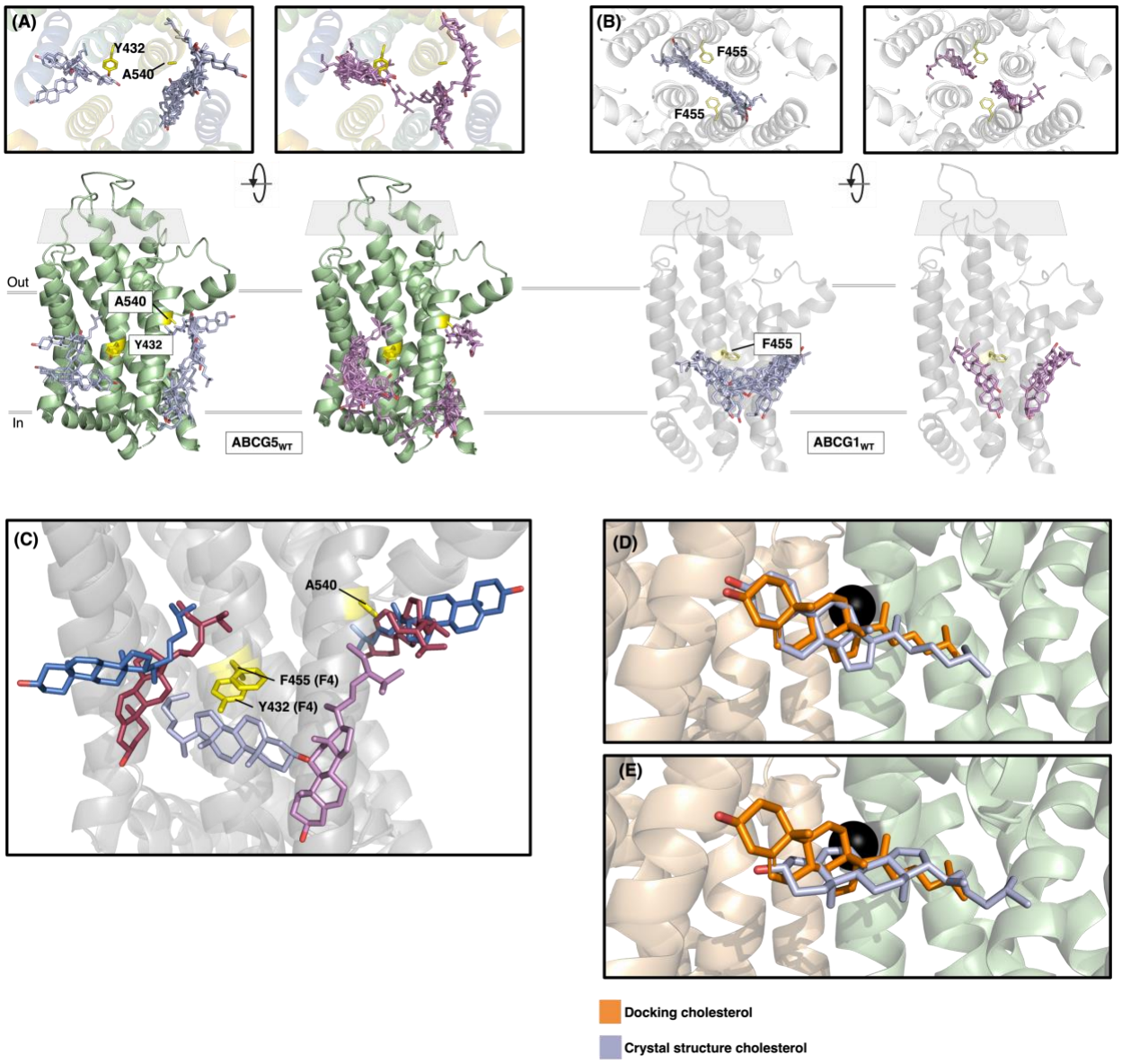

Figure 3. Cholesterol and stigmasterol docking in ABCG5/G8 and ABCG1. (A-B) Cholesterol (pale blue, left) and stigmasterol (pale purple, right) are bound to either side of the interface between the two dimers. **(A)** Cholesterol or stigmasterol in ABCG5/G8 docks differently on either side (shown only ABCG5 here). *Left of Y432*, cholesterol docks in three conformations: lightly angled upwards above Y432, horizontal on the X-axis below Y432 and vertical. Stigmasterol (right) poses to the left of Y432 has a "C" shaped pattern that surrounds Y432. *Right of Y432*, cholesterol binds in a continuous pattern, starting at A540 and ending at the lower edge of the transmembrane domain (TMD). A single cholesterol conformation binds horizontally near A540. Stigmasterol binds in two separated clusters with the top cluster showing horizontal poses ahead of A540 and the bottom cluster containing horizontally oriented sterols. **(B)** On ABCG1, either cholesterol or stigmasterol includes similar docking poses on both sides. The sterols are angled towards the putative sterol binding cavity on the cytoplasmic end of the bilayers. Given similar binding pattern, more cholesterol poses are obtained than stigmasterol. **(C)** Top sterol poses on

both transporters are illustrated as a superposition**.** ABCG1 cholesterol and stigmasterol are colored pale blue and pale purple respectively. ABCG5/G8 cholesterol and stigmasterol are colored dark blue and dark red respectively. In general, sterols in ABCG5/G8 dock higher, near the orthogonal sterol-binding site, whereas sterols in ABCG1 binds under F455 (below F4 of the phenylalanine highway). **(D, E)** The cholesterol docking pose (orange) is aligned with either cholesterol in the asymmetric unit of the crystal structure (light blue) with an RMSD of 0.4 Å (D) and 0.9 Å (E).

To analyze sterol docking with ATP-bound structures, we performed the analysis on an ATP-bound ABCG1 and a homology model of ATP-bound ABCG5/G8 (see Materials and Methods) (Manolaridis et al., 2018). Surprisingly, given the same docking grid as used for apo structures, sterol docking on the ATP-bound ABCG1 or ABCG5/G8 only showed clusters on top of the extracellular domains of the extracellular-facing structures and far away from the PH (**Fig. 4A/B**). As current apo or ATP-bound structures of ABCG sterol transporters are rather limited to early and end states of catalysis (Lee et al., 2016; Skarda et al., 2021; Sun et al., 2021; Zhang et al., 2021), the sterol poses as observed here may represent the post-efflux conformations as the hydrophobic valve has already been resealed in these ATP-bound structures. For this reason, binding sites within the protein were unable to be detected and subsequently docked. Our data thus emphasize the need for occluded turnover state models, as seen in ABCG2 models (Yu et al., 2021).

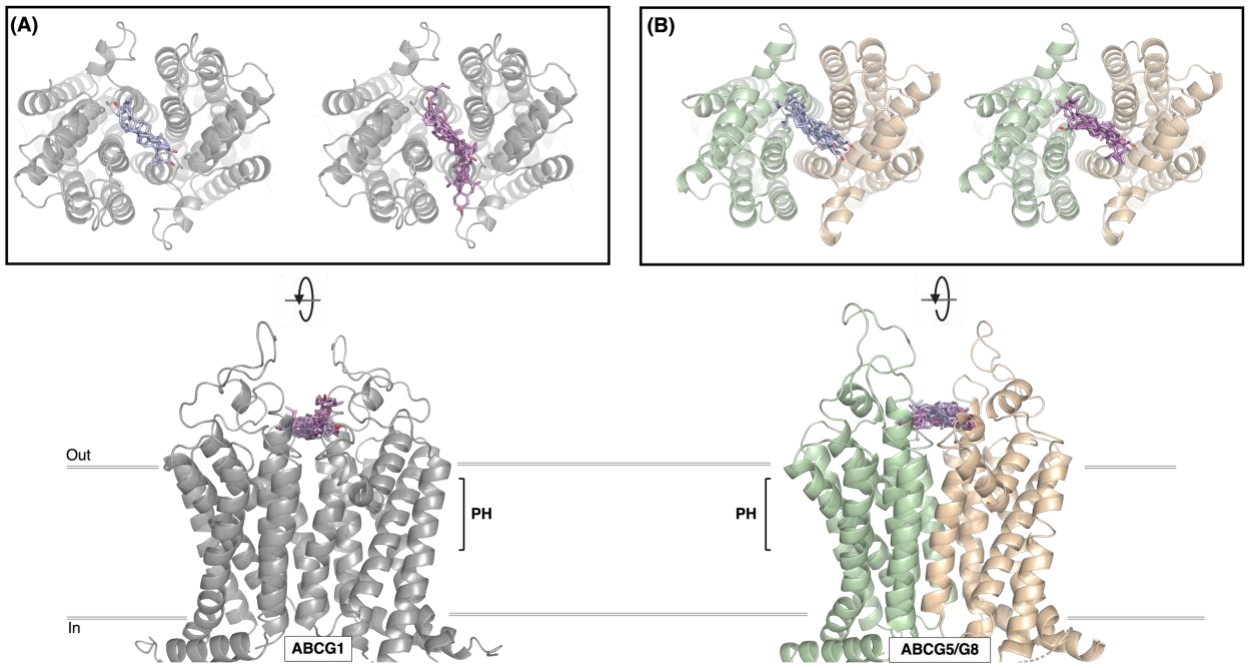

Figure 4. (A,B) Sterol docking on ATP-bound ABCG1 (A) and ABCG5/G8 (B) models. ABCG1 in gray; ABCG5/G8 in green and tan. Cholesterol (blue) and stigmasterol (violet) docked shown in a front view (lower) and a top-down view (upper). In brackets is the extent of the phenylalanine highway (PH) within the transmembrane domain (TMD) of the protein.

2.4 Sterol selectivity by ABCG1 and ABCG5/G8:

Among mammalian ABCG sterol transporters, ABCG5/G8 is known to promote absorption of cholesterol but not dietary sterols in the gastrointestinal tract (Berge et al., 2000). To study such sterol selectivity, we analyzed the distributions of the sterol-binding poses from the docking experiments by using ABCG1 and ABCG5/G8 as model systems. On ABCG1, cholesterol cluster was gathered uninterruptedly around F455, *i.e.*, F4 of PH, and docked similarly on both sides of the transporter-membrane interface. The sterol cloud is angled towards the putative sterol binding cavity at the NBD-TMD interface, in the membranes lower leaflet. (**Fig. 3A, bottom**). Stigmasterol equally shows the same angling into the binding site, but with reduced possible poses when compared to cholesterol on ABCG1 (**Fig. 3B, bottom**). The largest number of positions for cholesterol or stigmasterol are located immediately below the PH and above the NBD-TMD

interface, suggesting a common sterol-binding cavity in ABCG sterol transporters. However, the orientation the hydroxyl group on the sterols is not necessarily exposed to the aqueous milieu (**Fig. 3A/B, bottom**).

On the ABCG5-dominant side of ABCG5/G8, stigmasterol binds in two clusters partitioned between each monomer, leaving a gap in the middle, which is opposite to the continuous cloud as revealed by cholesterol (**Fig. 3A/B, top**). In general, there are more possible binding poses in the vicinity of ABCG5$_{A540}$ and ABCG8's PH, where interestingly all sterol molecules appear to orient in a similar direction, *i.e.*, the hydroxyl group pointing to the NBD-TMD interface. On the other hand, on the ABCG8-dominant side and near F4 of ABCG5's PH, the sterol molecules are oriented in various but seemingly unspecific directions (or conformations) (**Fig. 3A/B**). When compared to cholesterol which binds in two separate pockets (**Fig. 3A, top**), stigmasterol has three binding pockets across both sides of the transporter-membrane interfaces (**Fig. 3B, top**). Interestingly, the highest clusters of stigmasterol and cholesterol are located on the opposite sides of the transporter, suggesting preferred association of sterol species on either side of the transporter-membrane interface.

ABCG1$_{F455}$ and ABCG5$_{Y432}$ are at the equivalent position F4 of the PH. When comparing the sterol binding patterns around these key residues, more cholesterol poses can be found around ABCG1$_{F455}$ in an increasingly linear shape, while more stigmasterol poses were observed around ABCG5$_{Y432}$ in a "C" shape (**Fig. 3A/B**). In the nucleotide-free structures as used for analysis here, sterol binding in general is positioned more towards the orthogonal sterol-binding site in ABCG5/G8 than in ABCG1. Sterol poses in ABCG1 cluster closer to the central cavity, around PH's F4, while sterols bind ABCG5/G8 closer to the transporter-membrane interface (**Fig 3C**). The sterols of the top binding poses all have hydroxyl groups pointing outwards and away from

PH's F4 position. Interestingly, the cholesterol molecules are similarly angled in both ABCG1 and ABCG5/G8, *i.e.,* in parallel to the lipid bilayers.

2.5 Alteration of ABCG5/G8 cholesterol-binding activity by the LOF mutant A540F:

By exploiting the LOF mutant A540F, *in vivo* and *in vitro* functional studies support the notion that it is exposed to the orthogonal cholesterol-binding site (Lee et al., 2016; Xavier et al., 2020) (**Fig. 2**). Using molecular docking and homology modelling, it is possible to develop hypotheses for the structural basis of how this mutation impacts ABCG5/G8 function. In this study, we analyzed the effects of inducing the A540F mutation on the binding positions of cholesterol as compared to in WT ABCG5/G8 (**Fig. 5**). In the WT protein, the cholesterol cloud stretches from proline 415 (P415, end of the connecting helix of ABCG8) to A540 (**Fig. 5A**), with one of the top poses being the orthogonal sterol adjacent to A540. The remaining top-three are vertically oriented, exposing the hydroxyl group to the orthogonal sterol-binding site (**Fig. 5B, right & Fig. 5C**). Using a homology model containing the A540F mutation, the second and third best binding positions were missing, leaving a gap between PH's F4 and the orthogonal sterol-binding site (**Fig. 5B, left & 5C**). As mutation was induced, the orientation of the orthogonal cholesterol is flipped 180° at the sterol-binding site (**Fig. 5D/E**), and the remaining non-top three poses have their hydroxyl groups pointing to the cytoplasmic side of the lipid bilayer (**Fig. 5B**). Overall, lower number of different cholesterol poses were docked on the mutant as compared to the WT protein. The microenvironment surrounding the orthogonal cholesterol on A540F mutant are highlighted in **Figure 5E**, showing that the phenylalanine substitution prevents the interactions between the cholesterol and polar residues (*e.g.*, $ABCG8_{T430}$) that may attract the hydroxyl group in the WT protein.

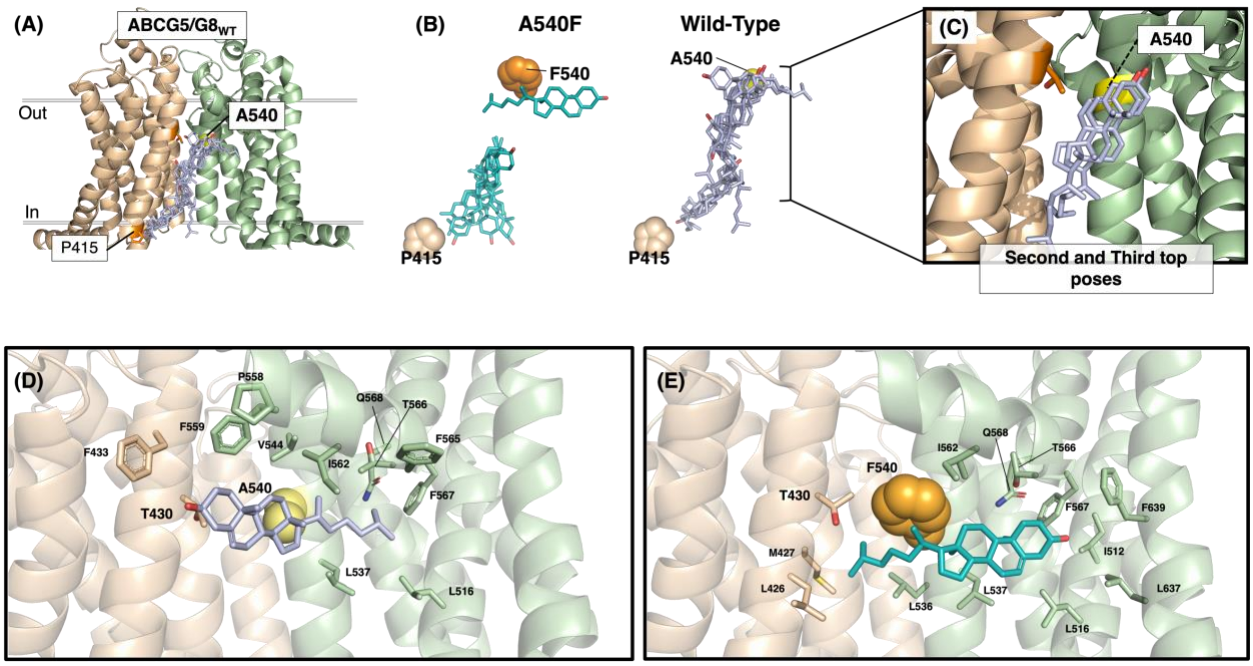

Figure 5. Wild-type and mutant A540F ABCG5/G8 docking predictions. (A-C) ABCG5 and ABCG8 are colored in green and tan respectively, and the cholesterol docking on WT results are shown in (A). In comparison, WT docking is shown in pale blue while mutant is shown in teal (B). Residues $ABCG5_{A540}$ and $ABCG8_{P415}$ are highlighted in tan and orange respectively for the orientation (B), showing that WT has a continuous cholesterol binding pattern from A540 to P415 while the mutant has a break in the docking prediction, separating the two clusters. Two of the top 3 poses in the wild type docking appear to be missing in the A540F mutant (C). **(D, E)** The micro-environment surrounding cholesterol highlights sterol-protein interaction. Residues are shown as sticks. From left to right, ABCG8: L426, M427, T430; ABCG5: F559, F540, L536, I562, L537 Q568, T566, F567, L516, L637. The side chain of F540 is shown in spheres to highlight the mutation.

2.6 Lower transmembrane sterol-binding cavity in ABCG5/G8:

The recent cryo-EM structural determination of ABCG1 suggested a cholesterol-binding cavity in the cytoplasmic leaflet of the bilayer (Skarda et al., 2021; Sun et al., 2021). The protein's surface within the binding cavity in ABCG1 shows a narrow gap that is wider than corresponding cavity found in ABCG5/G8 (**Fig. 6A**); additionally, this cavity is located immediately below F4 of the PH (**Fig. 6B**). In the WT proteins, $ABCG5_{Y432}$ and $ABCG8_{N564}$ are separated by 4.0 Å, suggesting a weak hydrogen bonding, whereas the equivalent positions in $ABCG1_{F455}$ and $ABCG1_{P558}$ can not for hydrogen bonds and are separated by 6.9Å. We created an ABCG5/G8

homology model that consists of mutations ABCG5$_{Y432F}$ and ABCG8$_{N564P}$ to mimic an ABCG1-like cavity. The interaction between the mutant residues in ABCG5/G8 are at a similar distance and positions to the corresponding residues in ABCG1 (**Fig. 6B/C**). This distance is significantly widened from 4.0 Å to 6.9 Å in the mutant. Due to the increased distance between the residues, the double mutant lacks the ability to form a hydrogen bonding and results in a deeper cavity than WT. We then performed sterol docking analysis on this double-mutant model and analyzed the possible sterol conformations in this cytoplasmic sterol-binding cavity. In the WT, stigmasterol appears to bind more readily than cholesterol, where the cluster of docked stigmasterol poses is much bigger than the cholesterol cloud (**Fig. 6D/E**). Both sterol clouds semi-encircle Y432 in a "C" shape. When Y432 is mutated to phenylalanine, the number of docked sterols decreased significantly as compared to the WT, simply localizing overhead of position 432 and suggesting lower sterol-binding ability in the mutant. Interestingly, the size of viable poses becomes more alike for either cholesterol or stigmasterol. Despite using ABCG5$_{Y432F}$/G8$_{N564P}$ mutations to mimic the width of the cavity found in WT ABCG1, the binding pattern in the mutant does not resemble that of ABCG1 (**Fig. 2A/B, bottom**), suggesting the possibility of either sterol transporter adopting multiple conformations to bind sterols throughout the transport cycle. Further analysis is necessary to define the role of these residues.

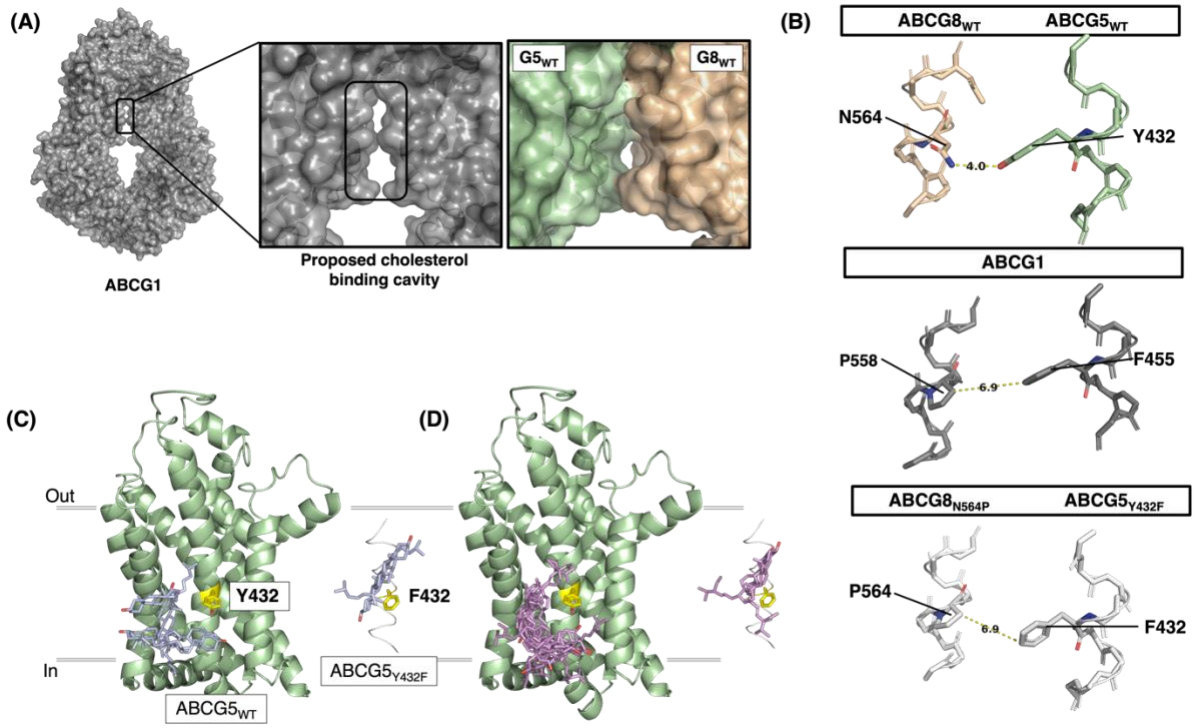

Figure 6. Lower transmembrane cavity in ABCG5/G8 and ABCG1 with cholesterol and stigmasterol docking on wild-type and double mutant (Y432F, N564P) ABCG5/G8. (A) ABCG1's (PDB ID: 7OZ1, gray) hollow transmembrane region was previously denoted as a putative cholesterol binding cavity contrasted with ABCG5(green)/G8(tan). All atoms are included (but not displayed) with the surface fit over the protein. **(B)** WT ABCG5/G8 (PDB ID: 7RJ7, green/tan) with residues Y432 and N564 shown as sticks. Distance between the two amino acids is ~4.0 Å, considered as weak hydrogen bonding. For the equivalent residues in ABCG1 (PDB ID: 7OZ1, gray), F455 and P558, they are ~6.9 Å apart, not sufficient of forming a hydrogen bond. A homology model of the double-mutant ABCG5/G8, shown in white, has Y432 and N564 substituted for phenylalanine and proline, respectively, as observed in ABCG1. **(C, D)** Cholesterol (blue) and stigmasterol (violet) docking was simulated on WT (green) and double mutant (white) ABCG5/G8, with only ABCG5 shown here. Yellow: residue 432 on ABCG5. Wild type has more potential binding poses than the double mutant that only binds a handful sterols above residue 432.

3. DISCUSSION

Atomic models of ABCG sterol transporters have provided the molecular framework to study how individual transporter proteins translocate different substrates. Yet, the location and methods by which these transporters bind sterols remains elusive and controversial. This is particularly true in the case of ABCG5/G8, which is believed to identify and bind plant sterols differently from cholesterol. Understanding how sterols binds on ABCG5/G8 and its homologs will allow us to study the impact of such sterol selectivity on the regulation of sterol transport. In this study, we have determined a cholesterol-bound crystal structure of ABCG5/G8, showing an orthogonal cholesterol binding on the ABCG5-dominant side at the transporter-membrane interface (**Fig. 2**). A mutant $ABCG5_{A540F}$ was previously demonstrated to downregulate biliary cholesterol efflux *in vivo* (Lee et al., 2016) and to inhibit sterol-coupled ATPase activity *in vitro* (Xavier et al., 2020). The crystal structure herein provides a structural evidence of this peripheral sterol binding site where a sterol molecule makes direct contact with the conserved $ABCG5_{A540}$ residue (**Fig. 2 & 5**). The sterol fits into an indented planar cleft within the upper region of the vestibule formed by the re-entry and the transmembrane helices. The captured cholesterol extends across the interfacial space, with its hydroxyl group forming a hydrogen bond with $ABCG8_{T430}$, while the hydrocarbon tail remains straight and in contact with hydrophobic residues on ABCG5, such as L516, L537, I562, F565 and F567 (**Fig. 5D**). We also showed an inhibition of the cholesterol-binding activity by the A540F mutant (**Fig. 2C**). The K_D value is similar for both WT and mutant proteins, echoing the similar K_M for sterol-coupled ATPase activity in previous studies, given the mutant suppressed ATP hydrolysis by ~90% (Xavier et al., 2020). Taken together with a 180° flipping of cholesterol by this mutant (**Fig. 5E**), current structural and functional data suggest a functionally defective conformation by this LOF mutant, inhibiting both sterol and ATP

associations to the transporter. The Hill coefficient was estimated as ~3, suggesting two more sterol molecules may interact with the proteins besides the one binding at A540. Further structural and functional studies will be necessary to determine how these sterols bind ABCG5/G8.

In a separate experiment, cholesterol was docked to the TMD of previously published ABCG5/G8 structures (PDB ID: 5DO7 or 7JR7) (Lee et al., 2016; Zhang et al., 2021), where one of the top-3 predicted poses binds to the transporter in similar conformation as revealed by the crystal structure (**Fig. 3D/E**). The core steroid rings and the hydroxyl group matched in similar tilt, although the hydrocarbon tail varied slightly with minimal rotation. The latter may be explained by its relatively high mobility, such that the deviation was expected. Using a homology model containing the A540F mutation, the large aromatic group in position 540 introduced steric hindrance, consequently disabling cholesterol docking onto the observed position as shown in the crystal structure or predicted docking on WT protein (**Fig. 2 & 3**). In addition, cholesterol docking with the A540F mutant resulted in a loss of top-3 poses as seen on the WT protein. Altogether, past and present data support the existence of an orthogonal cholesterol binding site located around residue $ABCG5_{A540}$, and the orthogonal sterol poses may be part of intermediate states of sterol-translocation trajectory along the TMD.

Via a protein sequence analysis of primarily mammalian ABCG transporters, we have identified a structural motif, "phenylalanine highway" along the TMH2 that consists of conserved aromatic residues (usually phenylalanine) (**Fig. 1**). This motif is flanked by two highly conserved aromatic residues (*i.e.*, positions F1 and F4), where position F4 appears to involve in sterol capturing from the cytoplasmic end of the membranes (**Suppl Fig. 1)** and the PH may provide a pathway for docked sterols to enter the dimer's interface (**Fig. 3**). Although not fully defined, certain PH residues are believed to form a molecular clamp previously shown to mediate π–π

interactions with sterol molecules (Gose et al., 2020; Manolaridis et al., 2018; Orlando and Liao, 2020; Taylor et al., 2017). As substrates for ABCG tend to be polycyclic with more or less an aromatic group that can interact with aromatic amino acids, the PH motif possibly serves as a conserved molecular clamp of ABCG sterol transporters (**Fig. 1C**). The clamp-like role of the lower PH terminus was recently suggested by structural studies of ABCG1 and ABCG2. The ATPase activity of ABCG1 was inhibited by $ABCG1_{F455A}$ mutation (Sun et al., 2021), while ABCG2-driven drug efflux was downregulated by $ABCG2_{F439A}$ mutation (Gose et al., 2020). Interestingly, mutation $ABCG2_{F439Y}$ or $ABCG2_{F439W}$ did not hamper the efflux function, emphasizing the importance of aromatic residues in contributing to a substrate-binding route from the inner leaflet of the membranes (Gose et al., 2020). In ABCG5/G8, while the clamp-like function of $ABCG5_{Y432}$ has yet to be showcased, our docking analysis and a previous *in vivo* data suggest its biochemical nature as a key feature for the transporter function, presumably sterol binding. In this study, a double-mutant model ($ABCG5_{Y432F}$/$ABCG8_{N564P}$) revealed a loss of the ability to form a hydrogen bonding at the TMD dimer interface (**Fig. 6B**) and a deeper cavity was formed to imitate ABCG1, yet the overall binding patterns were adversely affected (**Fig. 6D/E**). This alteration in binding conformations and obstruction of the molecular clamp may help explain why *in vivo*, $ABCG5_{Y432A}$/$ABCG8_{WT}$ caused a significant decrease in biliary cholesterol efflux (Lee et al., 2016). The mutations we had modelled retained the aromatic group; the *in vivo* data thus suggested a loss of the molecular clamp at the lower PH terminus. It is important to note that $ABCG5_{Y432}$ is also part of the TMD polar relay network (Khunweeraphong et al., 2020; Xavier et al., 2020). Unlike the ABCG8 equivalent ($ABCG8_{F461}$), $ABCG5_{Y432}$ may play a dual role in the sterol binding/translocation and the allosteric regulation that couples ATPase and sterol-transport activities (Xavier et al., 2020).

The upper PH terminus (*i.e.*, ABCG5$_{Y424}$ and ABCG8$_{F453}$) lies immediately under the hydrophobic valve (**Fig. 1D/E**), suggesting a cooperativity between PH's F1 position and the hydrophobic valve in the sterol-transport function. ABCG5$_{Y424}$, ABCG8$_{F453}$ and ABCG1$_{F447}$ all extend their side chains towards the valve's aromatic residues, forming aromatic-aromatic interactions as suggested previously (Sun et al., 2021). In ABCG1 and ABCG4, the di-phenylalanine valve may grant the possibility of aromatic interactions between the neighboring six phenylalanine residues. In contrast, the leucine and methionine from ABCG5/G8's hydrophobic valve provide an asymmetric gating of sterol transport, as opposed to the symmetric valve in ABCG1 or ABCG4. In ABCG2, the lack of any phenylalanine within its di-leucine valve denies π–π interactions, although ABCG2$_{F431}$ (PH's F1) was shown to engage in drug-protein interactions with ABCG2 inhibitors (Jackson et al., 2018). Position F2 in the PH is moderately conserved **(Fig. 1A)**, although residues at this position has been proposed to involve sterol interactions, as suggested by decreased cholesterol efflux in the presence of ABCG1$_{F448A}$ mutant (Xu et al., 2022) or drug interaction in ABCG2 (Nagy et al., 2021). Interestingly, such a PH-like motif may not be limited to ABCG sterol transporters. We have observed similar phenylalanine spacing on the structures of other cholesterol-binding or -transport proteins, including ABCA1, ABCA7, SIDT1, SIDT2, PTCH1, and NPC1 (**Suppl Fig. 4**) (Harris et al., 2021; Jumper et al., 2021; Long et al., 2020; Qi et al., 2018; Qian et al., 2017). The PH structural motif may be more common than expected, and further studies will be needed to define its functional roles.

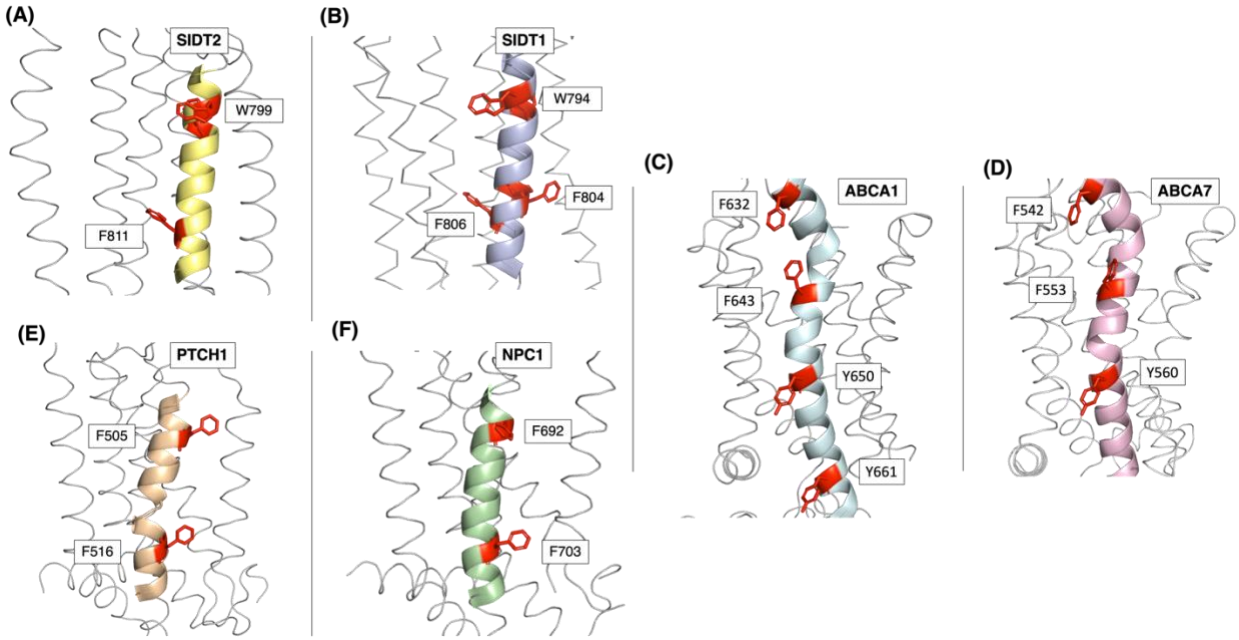

Supplementary Figure 4. Aromatic amino acid pattern in non-ABCG lipid transporters. Conserved aromatic residues along the putative (or observed) sterol-binding/interacting TMH (cartoon presentation) show a similar pattern of phenylalanine highway as observed in ABCG transporters. SIDT2 (**A**, yellow), SIDT1 (**B**, dark blue), ABCA1 (**C**, light blue), ABCA7 (**D**, pink), PTCH1 (**E**, orange) and NPC1 (**F**, green). The aromatic amino acids: phenylalanine, tyrosine and tryptophan are highlighted in red sticks. Only the most central and luminal helices are modelled in detail.

The docking experiments in this study have allowed us to analyze different binding profiles of cholesterol or stigmasterol on ABCG1 and ABCG5/G8 (**Fig. 3**). Previous *in vivo* studies showed that stigmasterol efflux by ABCG5/G8 was the fastest among dietary plant sterols (Yu et al., 2004); hence stigmasterol was used to analyze phytosterol/plant sterol binding to ABCG transporters. Both proteins share cholesterol as a substrate yet deviate in phytosterol transporting abilities. ABCG5/G8 is a known phytosterol transporter, and each transporter-membrane interface has a distinct selectivity for one of the two docked sterols (**Fig. 3A/B**). In comparison, ABCG1 showed similar binding conformations between stigmasterol and cholesterol, with a decreased amount of stigmasterol binding poses on ABCG1 than ABCG5/G8. Together, our results indicate that sterol selectivity not only occurs on the opposite transporter-membrane interfaces but also differentiate

ABCG5/G8 from other ABCG sterol transporters. In addition, our simulation showed the hydrocarbon tail of sterol molecules leading to the PH along with the TMD dimer interface, rather than the hydroxyl group as seen in previous cryo-EM structures of ABCG1 (Sun et al., 2021). However, at least one docking pose on the ABCG8-dominant side horizontally points its hydroxyl group to the dimer interface, similar to that of a recent cryo-EM structure **(Suppl Fig. 5)**. We speculate that the cholesterol orientation as seen in the cryo-EM structures may represent an intermediate cholesterol-binding state among the docked poses (**Fig. 5**).

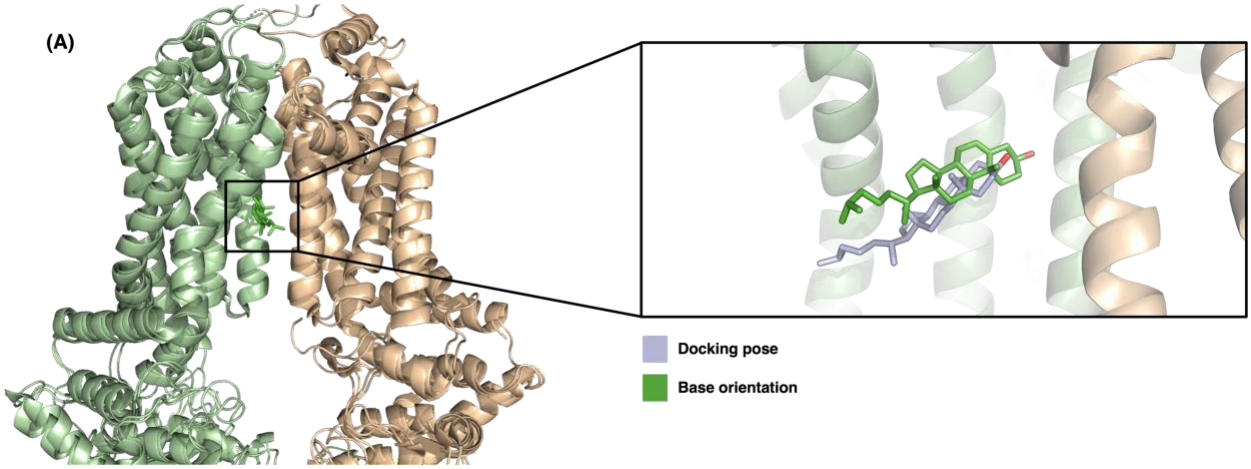

Supplementary Figure 5. ***Left.*** **Crystal structure of ABCG5/G8** (PDB ID: 5DO7) aligned with cryo-EM structure (PDB ID: 7R8D). *Right.* Comparison of cholesterol docking pose (light blue) with the cholesterol (green) in the cryo-EM structure (Sun et al., 2021).

Studies on cholesterol redistribution in lipid rafts have suggested a TMD sterol access site in ABCG1 (**Fig. 4**) (Ristovski et al., 2021; Sano et al., 2014, 2007). Theoretically, ABCG1 intakes sterols from enriched lipid microdomains, relocating them towards the surrounding sterol-deprived membranes. The docking pattern follows the amphipathic nature of the lipid bilayers with cholesterol's polar head localizing around the cytoplasmic matrix **(Fig. 3)**, where. cholesterol's hydroxyl group is believed to generate hydrogen bonds with the surrounding polar lipid regions, orienting the sterols head towards the hydrophilic region (Ermilova and Lyubartsev, 2019). Our

docking analysis suggests ABCG1's apparent preference for the inner leaflet sterols (Sano et al., 2014), where the transporters then translocate cholesterol to the upper leaflet, similar to the recently proposed mechanism (Skarda et al., 2021; Xu et al., 2022). In ABCG5/G8, both crystallographic and docking results indicated that sterol binding is not limited to the TMD cavity open towards to the cytoplasmic side, but an orthogonal sterol-binding state is a possible intermediate state to drive sterol efflux. As the TMD dimer interface in ABCG5/G8 is much narrower than that in ABCG1, it is possible that ABCG5/G8 similarly uptakes sterol substrates as ABCG1. Still, sterols would need to undergo a series of yet-to-be characterized movements from their longitudinal orientations to an orthogonal binding state as shown in the cholesterol-bound structure (**Fig. 2 &3**). Among ABCG5/G8 substrates, plant sterols may show higher binding preferences as suggested by stigmasterol poses (**Fig. 3**).

In conclusion, our crystallographic and computational analysis have highlighted possible regions of sterol binding and interactions on ABCG5/G8. This study shows a conserved phenylalanine highway motif on TMH2 that may play an essential role in sterol recruitment and binding and a crystal structure revealing an orthogonal cholesterol bound on the ABCG5-dominant transporter-membrane interface, consistent with the leading cholesterol poses predicted by molecular docking. The docking analysis of cholesterol and stigmasterol also suggested the asymmetric sterol-binding potential on ABCG5- and ABCG8-dominant transporter-membrane interfaces, and difference in sterol-docking patterns may contribute to different substrate specificity between ABCG1 and ABCG5/G8. Further structural and functional studies will reveal more insight into sterol selectivity and translocation trajectory by ABCG sterol transporters.

4. MATERIALS AND METHODS

4.1 Protein purification and crystallization

For purification of human WT ABCG5/G8 from *Pichia pastoris* yeast, we have followed the procedures based on our previously reported protocol (Lee et al., 2016). With minor modifications, the procedures are briefly described in the following. For each purification, six litres of yeast cell culture were used for ~200 mL of the microsomal membrane preparation at the total protein content of ~10 mg/mL. The membranes were solubilized by equal volume of the solubilization buffer (50 mM Tris-HCl, pH 8.0, 100 mM NaCl, and 10% glycerol, 2% (w/v) β-dodecyl maltoside (β-DDM, Anatrace), 0.5% (w/v) cholate (Sigma-Aldrich), 0.25% (w/v) cholesteryl hemisuccinate Tris (CHS-Tris, Anatrace), 5 mM imidazole, 5 mM β-mercaptoethanol (β-ME), 2 μg/ml leupeptin, 2 μg/ml pepstatin A, 2 mM PMSF). Insoluble membranes were removed by ultracentrifugation, and the solubilized supernatant was treated with a final concentration and 0.1 mM Tris (2-carboxylethylcarboxyethyl) phosphine (TCEP). Following that, tandem affinity chromatography was performed. The soluble membrane proteins were separated using a 20-mL nickel-nitrilotriacetic acid (Ni-NTA) column. Then, the peak fractions of ABCG5/G8 from the Ni-NTA eluates were mixed with the equal amount of CBP column wash buffer (50 mM HEPES, pH 7.5, 100 mM NaCl, 0.1% (w/v) β-DDM, 0.05% (w/v) cholate, 0.01% (w/v) CHS (Steraloids), 0.1 mM TCEP ,1 mM $CaCl_2$, 1 mM $MgCl_2$) and then loaded onto a 5-mL CBP column. The CBP column was washed sequentially to exchange detergents to DMNG, and ABCG5/G8 proteins were finally collected using an elution buffer (50 mM HEPES, pH 7.5, 300 mM NaCl, 2 mM EGTA, 0.1% (w/v) DMNG, 0.05% (w/v) cholate, 0.01% (w/v) CHS, 1 mM TCEP). The N-linked glycans and the CBP tag were cleaved by endoglycosidase H (Endo H, ~0.2 mg per 10–15 mg purified protein, New England Biolabs) and HRV-3C protease (~2 mg per 10–

15 mg purified proteins) for overnight at 4 °C. The CBP tag-free proteins were further purified by gel filtration chromatography using an ÄKTA Purifier and a Superdex 200 30/100 GL column in the buffer containing 10 mM HEPES, pH 7.5, 100 mM NaCl, 0.1% (w/v) DMNG, 0.05% (w/v) cholate, 0.01% (w/v) CHS. The peak fractions were pooled together and treated by reductive methylation. The methylated proteins were relipidated by overnight incubation with 0.5 mg/ml DOPC: DOPE (3:1, w/w) and further purified by a 2-mL Ni-NTA column, followed by iodoacetamide treatment for cysteine alkylation. The relipidated proteins were treated with 1 mM AMPPNP (sodium salt, Roche) for overnight at 4 °C and desalted with a PD-10 column. The desalted and lipidated proteins were incubated overnight with cholesterol (prepared in isopropanol) to a final concentration of ~20 μM, and protein precipitants were removed by ultracentrifugation for 10 min at 4 °C. Using 100 kDa cutoff filters, the supernatants were concentrated to a final protein concentration of 30-50 mg/ml and crystallized within a week.

Protein crystal growth was carried out by bicelle crystallization as described previously. Briefly, the cholesterol-treated ABCG5/G8 proteins were reconstituted into 10% DMPC/CHAPSO bicelles (lipids and detergents in a 3:1 (w/w) ratio, with the lipids containing 5 mol% cholesterol and 95 mol% DMPC). After that, the proteins and bicelle stock were gently mixed in a 1:4 (v/v) ratio, resulting in a final protein concentration of ~10 mg/ml. At 20 °C, the crystallization was done in a hanging-drop vapor diffusion technique by mixing protein/bicelle preparation with equal-volume crystallization reservoir solution containing 1.8–2.0 M ammonium sulfate, 100 mM MES pH 6.5, 2–5% PEG400, and 1 mM TCEP. Protein crystals were harvested within 1-2 weeks of incubation by first submerging the crystals with 0.2 M sodium malonate and then flash-freezing the crystals in liquid nitrogen with Mitegen cryoloops.

4.2 Data collection of X-ray diffraction, structural determination and refinement

X-ray diffraction data were collected using beamlines 19-ID on a Quantum 315r detector at the Advanced Photon Source (APS). Scaling and integration of three datasets were carried out by HKL2000 software package, and the final data was scaled between 30Å and 4Å resolutions to ensure I/σ >1 (Otwinowski and Minor, 1997). Using Phaser program, we obtain the phase information and a structural solution by molecular replacement using a cryo-EM structure (PDB ID: 7JR7) as the initial template (Grayling, 2014; Zhang et al., 2021). Before model refinement by Phenix, the Phaser solution was corrected at the Walker A, the Walker B, and the Signature motifs by the more defined registry in the crystal structure (PDB ID: 5DO7) (Adams et al., 2010; Lee et al., 2016). The initial refinement resulted in a refined model with Rfree and Rwork of 0.338 and 0.309, respectively. Close inspection of the Fo-Fc map, two orthogonal electron densities that clearly include the nature of polycyclic rings were observed between the crystallographic dimer interface and on the ABCG5-dominant side where each electron density is within the van der Waals' distance from $ABCG5_{A540}$. No such electron densities were observed on ABCG8-dominant side. We thus modeled a cholesterol molecule per electron density, and we refined the structure in the presence of one cholesterol molecule on each ABCG5/G8 heterodimer by testing a series of sterol orientations using the program COOT (Emsley and Cowtan, 2004). Following our final refinement, Rfree and Rwork were determined to be 0.302 and 0.244, respectively. The model quality was validated by MolProbity as implemented in Phenix (Adams et al., 2010; Chen et al., 2010). As a note, given the proteins were co-crystallized with AMPPNP, we were not able to observe obvious electron densities for the nucleotides from the current datasets at the current resolution.

4.3 Protein sequence analysis

All FASTA files were acquired using PSI-BLAST (position-specific iterated basic local

alignment search tool) as implemented in the NCBI protein sequence database. All queries were acquired such that the organism belonged to the Mammalia family, and all partial and incomplete queries were filtered out. FASTA sequences were then surveyed one by one to ensure that the search criteria were executed properly, and no incomplete sequences were passed. FASTA sequences were acquired for ABCG1, ABCG2, ABCG4, ABCG5, and ABCG8 (P45844, Q9UNQ0, Q9H172, Q9H222, Q9H221) with the following PSI-BLAST search query: *"ABCXY"[Gene] AND "Mammalia"[Organism] NOT "partial"[All Fields],* Whereby X denotes the ABC subfamily, and Y denotes the member protein. Including 250-300 species, all alignments and analyses were run locally using the Bio Python repository (Cock et al., 2009). A multiple sequence alignment (MSA) was conducted using all the FASTA sequences using a BLOSUM62 substituation matrix (Henikoff and Henikoff, 1992), ClustalW (Thompson et al., 1994) or PROMALS3D (Pei et al., 2008). To score conservation, alignment files were made of the FASTA sequence library using the Multiple Sequence Comparison by Log-Expectation (MUSCLE) tool (Edgar, 2004). To generate a consensus sequence, a “dumb consensus” was conducted with a default threshold of 70% and a required multiple of 1. Consensus sequences were acquired for mammalian ABCG1, ABCG2, ABCG4, ABCG5, and ABCG8. Consensus sequences for each protein subfamily and member were compared to one another to determine highly conserved amino acids and amino acid sequences. For example, the amino acids present in the consensus sequence of ABCG1 was individually aligned to ABCG2, ABCG4, ABCG5, and ABCG8. Conservation scores above the set threshold (80%) were extracted for analytical purposes. An 80% similarity threshold, as opposed to 70%, was used using AMAS method of multiple sequence alignment because this analysis compared two consensus sequences together, 80% was chosen arbitrarily to ensure the amino acids chosen were highly similar without extracting ambiguous amino acid

(Livingstone and Barton, 1993). For further analysis, the results from the conservation scores were compared to each other (*i.e.,* the conservation scores of ABCG5 and ABCG2 was compared to conservation scores of ABCG5 and ABCG8). This was done across all comparisons to generate a comprehensive list of the amino acids that are conserved across all subfamily and member combinations. The same procedure was used to analyze ABCA1, ABCA7, SIDT1, SIDT2, PTCH1, and NPC1, of which experimental structures have been reported (Jumper et al., 2021; Long et al., 2020; Qi et al., 2018; Qian et al., 2017).

4.4 Homology Modelling

UCSF Modeller was used for homology modelling (Webb and Sali, 2014). The sequence alignment was created between the template and the mutant sequences using PROMALS3D (Pei et al., 2008). The template is the currently accepted PDB ID: 5DO7 in conjunction with X-ray data to create a more accurate model with a better energy DOPE (discrete optimized protein energy) scores. The mutant sequences included $ABCG5_{Y432F}$, $ABCG8_{N564P}$ and $ABCG5_{A540F}$. After the alignment, UCSF Modeller was used to generate 400 models and to rank them based on their DOPE scores. The best model was taken and visualized using PyMOL or UCSF Chimera. For the ATP-bound model, the cryo-EM structure of ATP-bound ABCG2 E211Q (PDB ID: 6HBU) was used as the template (Manolaridis et al., 2018). 100 models were generated with MODELLER, and the model with the best DOPE score was used for the sterol docking experiments in this study. All models were evaluated using MolProbity web server (Chen et al., 2010) to ensure no severe geometric violation in the Ramachandran plot (Williams et al., 2018).

4.5 Protein and ligand model preparation for docking

Protein models ABCG1, ABCG2, ABCG5/G8, PTCH1, NPC1, ABCA1 and PDR5 gathered from RCSB PDB database, PDB ID: 7OZ1/7R8D, 6VXI/6VXF/6VXJ,

5DO7/7R8E/7JR7, 6OEU, 6UOX, 5XJY, 7P03, respectively. ABCG4, White protein, ABCA7, SIDT1/2 structures were downloaded from AlphaFold2 predictions (Harris et al., 2021; Jumper et al., 2021; Lee et al., 2016; Long et al., 2020; Orlando and Liao, 2020; Qi et al., 2018; Qian et al., 2017; Skarda et al., 2021; Sun et al., 2021; Zhang et al., 2021). Regions of interest in these proteins had very high confidence scoring (pLDDT>90). Visualization of the structures done through PyMOL and Chimera. Double mutant $ABCG5_{Y432F}$ and $ABCG8_{N564P}$ and $ABCG5_{A540F}$ were induced and modelled in MODELLER based on PDB ID: 5DO7. The proteins docked (ABCG1, ABCG5/G8, ATP-bound, ABCG5/G8 mutants) were cut at the elbows, excluding the nucleotide-binding domain due to the large size of the full protein (>999 amino acids). Cholesterol was gathered from PDB ID: 7R8D, while stigmasterol was obtained in PubChem (Sun et al., 2021). ABCG2 ligands used for docking (imatinib and SN38) were previously modelled within the structure (Jackson et al., 2018; Orlando and Liao, 2020). Dunbrack 2010 rotamer library (Shapovalov and Dunbrack Jr, 2011) and ANTECHAMBER (Wang et al., 2006) were used in dockprep charge and hydrogen bond additions.

4.6 Molecular Docking

UCSF Dock6.9 (Allen et al., 2015) was utilized through SBGrid (Morin et al., 2013) to perform molecular docking. UCSF Chimera (Pettersen et al., 2004) was used as the graphic software for the simulated models. Protein binding site was determined by “sphgen” estimation specified at 10 Å distance from the ligand, located roughly in the centre of the protein in ABCG transporters. The “gridbox” and “grid” were generated and analyzed prior to the dock. To avoid potential mixing-up, we first performed docking with each sterol ligand on either side of transporter-membrane interface, whose results were consistent with those when placing the ligands at the centre of the TMD interface. Grid was built at a distance of 8 Å from the selected “sphgen”

spheres, and ligand's energy was minimized through minor conformational changes. A flexible docking procedure was then followed by calculation of 1000 or 5000 orientations, yielding no difference in results. The best scoring poses were compiled and individually viewed through UCSF Chimera's viewdock tool, these were then ranked by van der Waals energy (vdw_energy) and root mean square deviation (RMSD). Interacting amino acids were identified and plotted by both Chimera and PyMOL (Pettersen et al., 2004).

To validate our protocol for sterol docking on ABCG1 or ABCG5/G8, we performed a control experiment using ABCG2 and three of its known drugs (i.e., imatinib, and SN38) (Orlando and Liao, 2020). Using a previously published ABCG2 structure (PDB ID: 6FFC, 6VXH and 6VXJ), ABCG2 was docked with the drug ligand (one at a time) and weighed again against the originally modelled pose (Jackson et al., 2018). The simulated results showed consistent orientation of the drugs between predicted and experimental data, and the best pose for each drug fits the originally modelled ligand with the best RMSD and the lowest van vdw_energy value. The "best pose" in this study was therefore defined as the lowest van der Waal's (vdw) energy, which was used to rank all of the docking results.

4.7 Cholesterol binding assay

A direct cholesterol-binding assay using detergent-purified ABCG5/G8 was developed based on the previously described (Radhakrishnan et al., 2004). Briefly, 0.24µM of His-tagged WT ABCG5/G8, the mutant or the control protein (*i.e.*, BSA) was incubated with 0-4 µM of cholesterol that was prepared in the presence of [^{3}H]Cholesterol with a specificity of 110cpm/fmol (Perkein Elmer) in 50 µl of binding buffer containing 50mM Tris-HCl pH7.5, 100mM NaCl, and 0.05%(w/v) β-DDM (Anatrace), 0.05% (w/v) sodium cholate (Sigma-Aldrich), 1mM TCEP, 30µl of pre-equilibrated Ni-NTA bead (QIAGEN) on ice for overnight. The supernatant was removed

by centrifugation at 600 rpm for 1min in a bench-top centrifuge. The bead was extensively washed with 600 µl of ice-cold binding buffer plus 0.01% (w/v) CHS (Steraloids) for 4 times. To elute protein, 600 µl of binding buffer plus 0.01% (w/v) CHS and 200mM imidazole was added and incubated with the washed bead on ice for 30min. The bound [3H]Cholesterol was quantified by measuring the radioactivity of 500µl of elution fraction in a liquid scintillation counter (Perkin Elmer Tri-Carb 4910TR).

5. Data Availability

Diffraction data have been deposited in PDB under the accession code 8CUB.

AUTHOR CONTRIBUTIONS:

DF carried out docking analysis of ABCG transporters and other cholesterol-binding proteins; JYL performed crystallization and collected X-ray diffraction data; FR processed the X-ray data and determined the crystal structure. DF, MR and AS performed sequence analysis; MR and LD generated homology models. YY, JFC and JYL designed the cholesterol-binding assay; YY optimized the assay and analyzed the data. JYL oversaw the project, and DF, MR, FR, SS and JYL wrote the manuscript. All authors have read and agreed to the submitted version of the manuscript.

FUNDING:

This research was supported by a startup grant from the University of Ottawa, a Natural Sciences and Engineering Research Council Discovery Grant (RGPIN 2018-04070), a National New Investigator Award from the Heart and Stroke Foundation of Canada, and a Canadian Institutes of Health Research Project Grant (PJT-180640) to JYL.

ACKNOWLEDGEMENTS:

We thank the technical help from the staff of both the Common Equipment & Technical Services and the Protein Biophysics Core Facilities, as well as the critical feedback from Drs. Thomas Stockner, Gregory Graf, and Ms. Annahat Kochhar. We also thank Aiman Zein, Angelica Venes and Toka Hussein for technical assistance. This work is partially based on the theses that were submitted to fulfill in part the requirement for the degrees of Honors Bachelor of Science (DF & MR). FR is partially supported by an Academia Sinica-University of Ottawa Travel Support for Research Projects. The Advanced Photon Source is a US Department of Energy Office of Science User Facility operated for the Department of Energy Office of Science by Argonne National Laboratory (DE-AC02-06CH11357).

REFERENCES

Adams PD, Afonine P V, Bunkóczi G, Chen VB, Davis IW, Echols N, Headd JJ, Hung L-W, Kapral GJ, Grosse-Kunstleve RW, McCoy AJ, Moriarty NW, Oeffner R, Read RJ, Richardson DC, Richardson JS, Terwilliger TC, Zwart PH. 2010. PHENIX: a comprehensive Python-based system for macromolecular structure solution. *Acta Crystallogr D Biol Crystallogr* **66**:213–221. doi:10.1107/S0907444909052925

Allen JD, van Loevezijn A, Lakhai JM, van der Valk M, van Tellingen O, Reid G, Schellens JHM, Koomen G-J, Schinkel AH. 2002. Potent and Specific Inhibition of the Breast Cancer Resistance Protein Multidrug Transporter in Vitro and in Mouse Intestine by a Novel Analogue of Fumitremorgin C1. *Mol Cancer Ther* **1**:417–425.

Allen WJ, Balius TE, Mukherjee S, Brozell SR, Moustakas DT, Lang PT, Case DA, Kuntz ID, Rizzo RC. 2015. DOCK 6: Impact of new features and current docking performance. *J Comput Chem* **36**:1132–1156. doi:10.1002/jcc.23905

Austin DL, Weidong Y, V. AL, Tammy K, Yongming G, K. RA, D. RD. 1998. A multidrug resistance transporter from human MCF-7 breast cancer cells. *Proc Natl Acad Sci* **95**:15665–15670. doi:10.1073/pnas.95.26.15665

Berge KE, Hui T, A. GG, Liqing Y, V. GN, Joshua S, Peter K, Bei S, Robert B, H. HH. 2000. Accumulation of Dietary Cholesterol in Sitosterolemia Caused by Mutations in Adjacent ABC Transporters. *Science (80-)* **290**:1771–1775. doi:10.1126/science.290.5497.1771

Bojanic DD, Tarr PT, Gale GD, Smith DJ, Bok D, Chen B, Nusinowitz S, Lövgren-Sandblom A, Björkhem I, Edwards PA. 2010. Differential expression and function of ABCG1 and ABCG4 during development and aging. *J Lipid Res* **51**:169–181. doi:10.1194/M900250-JLR200

Chen VB, Arendall 3rd WB, Headd JJ, Keedy DA, Immormino RM, Kapral GJ, Murray LW, Richardson JS, Richardson DC. 2010. MolProbity: all-atom structure validation for macromolecular crystallography. *Acta Crystallogr D Biol Crystallogr* **66**:12–21. doi:10.1107/S0907444909042073

Cock PJA, Antao T, Chang JT, Chapman BA, Cox CJ, Dalke A, Friedberg I, Hamelryck T, Kauff F, Wilczynski B, de Hoon MJL. 2009. Biopython: freely available Python tools for computational molecular biology and bioinformatics. *Bioinformatics* **25**:1422–1423. doi:10.1093/bioinformatics/btp163

de Aguiar Vallim TQ, Lee E, Merriott DJ, Goulbourne CN, Cheng J, Cheng A, Gonen A, Allen RM, Palladino END, Ford DA, Wang T, Baldán Á, Tarling EJ. 2017. ABCG1 regulates pulmonary surfactant metabolism in mice and men[S]. *J Lipid Res* **58**:941–954. doi:https://doi.org/10.1194/jlr.M075101

Do TM, Noel-Hudson M-S, Ribes S, Besengez C, Smirnova M, Cisternino S, Buyse M, Calon F, Chimini G, Chacun H, Scherrmann J-M, Farinotti R, Bourasset F. 2012. ABCG2- and ABCG4-Mediated Efflux of Amyloid-β Peptide 1-40 at the Mouse Blood-Brain Barrier. *J Alzheimer's Dis* **30**:155–166. doi:10.3233/JAD-2012-112189

Edgar RC. 2004. MUSCLE: multiple sequence alignment with high accuracy and high throughput. *Nucleic Acids Res* **32**:1792–1797. doi:10.1093/nar/gkh340

Emsley P, Cowtan K. 2004. {\it Coot}: model-building tools for molecular graphics. *Acta Crystallogr Sect D* **60**:2126–2132. doi:10.1107/S0907444904019158

Ermilova I, Lyubartsev AP. 2019. Cholesterol in phospholipid bilayers: positions and orientations inside membranes with different unsaturation degrees. *Soft Matter* **15**:78–93. doi:10.1039/C8SM01937A

Ferreiro MJ, Pérez C, Marchesano M, Ruiz S, Caputi A, Aguilera P, Barrio R, Cantera R. 2018. Drosophila melanogaster White Mutant w(1118) Undergo Retinal Degeneration. *Front Neurosci* **11**:732. doi:10.3389/fnins.2017.00732

Gimpl G. 2016. Interaction of G protein coupled receptors and cholesterol. *Chem Phys Lipids* **199**:61–73. doi:10.1016/j.chemphyslip.2016.04.006

Gose T, Shafi T, Fukuda Y, Das S, Wang Y, Allcock A, Gavan McHarg A, Lynch J, Chen T, Tamai I, Shelat A, Ford RC, Schuetz JD. 2020. ABCG2 requires a single aromatic amino acid to "clamp" substrates and inhibitors into the binding pocket. *FASEB J* **34**:4890–4903. doi:10.1096/fj.201902338RR

Graf GA, Yu L, Li W-P, Gerard R, Tuma PL, Cohen JC, Hobbs HH. 2003. ABCG5 and ABCG8 Are Obligate Heterodimers for Protein Trafficking and Biliary Cholesterol Excretion*. *J Biol Chem* **278**:48275–48282. doi:https://doi.org/10.1074/jbc.M310223200

Grayling MJ. 2014. PhaseR: An R package for phase plane analysis of autonomous ODE systems. *R J* **6**:43–51. doi:10.32614/rj-2014-023

Harris A, Wagner M, Du D, Raschka S, Nentwig L-M, Gohlke H, Smits SHJ, Luisi BF, Schmitt L. 2021. Structure and efflux mechanism of the yeast pleiotropic drug resistance transporter Pdr5. *Nat Commun* **12**:5254. doi:10.1038/s41467-021-25574-8

Henikoff S, Henikoff JG. 1992. Amino acid substitution matrices from protein blocks. *Proc Natl Acad Sci U S A* **89**:10915–10919. doi:10.1073/pnas.89.22.10915

Jackson SM, Manolaridis I, Kowal J, Zechner M, Taylor NMI, Bause M, Bauer S, Bartholomaeus R, Bernhardt G, Koenig B, Buschauer A, Stahlberg H, Altmann K-H, Locher KP. 2018. Structural basis of small-molecule inhibition of human multidrug transporter ABCG2. *Nat Struct Mol Biol* **25**:333–340. doi:10.1038/s41594-018-0049-1

Jumper J, Evans R, Pritzel A, Green T, Figurnov M, Ronneberger O, Tunyasuvunakool K, Bates R, Žídek A, Potapenko A, Bridgland A, Meyer C, Kohl SAA, Ballard AJ, Cowie A, Romera-Paredes B, Nikolov S, Jain R, Adler J, Back T, Petersen S, Reiman D, Clancy E, Zielinski M, Steinegger M, Pacholska M, Berghammer T, Bodenstein S, Silver D, Vinyals O, Senior AW, Kavukcuoglu K, Kohli P, Hassabis D. 2021. Highly accurate protein structure prediction with AlphaFold. *Nature* **596**:583–589. doi:10.1038/s41586-021-03819-2

Khunweeraphong N, Mitchell-White J, Szöllősi D, Hussein T, Kuchler K, Kerr ID, Stockner T, Lee JY. 2020. Picky ABCG5/G8 and promiscuous ABCG2 - a tale of fatty diets and drug toxicity. *FEBS Lett* **594**:4035–4058. doi:10.1002/1873-3468.13938

Khunweeraphong N, Szöllősi D, Stockner T, Kuchler K. 2019. The ABCG2 multidrug transporter is a pump gated by a valve and an extracellular lid. *Nat Commun* **10**:5433. doi:10.1038/s41467-019-13302-2

Lee JY, Kinch LN, Borek DM, Wang Jin, Wang Junmei, Urbatsch IL, Xie XS, Grishin N V., Cohen JC, Otwinowski Z, Hobbs HH, Rosenbaum DM. 2016. Crystal structure of the human sterol transporter ABCG5/ABCG8. *Nature* **533**:561–564. doi:10.1038/nature17666

Lee M-H, Lu K, Hazard S, Yu H, Shulenin S, Hidaka H, Kojima H, Allikmets R, Sakuma N, Pegoraro R, Srivastava AK, Salen G, Dean M, Patel SB. 2001. Identification of a gene, ABCG5, important in the regulation of dietary cholesterol absorption. *Nat Genet* **27**:79–83. doi:10.1038/83799

Liqing Y, E. HR, Jia L-H, Klaus von B, Dieter L, C. CJ, H. HH. 2002. Disruption of Abcg5 and Abcg8 in mice reveals their crucial role in biliary cholesterol secretion. *Proc Natl Acad Sci* **99**:16237–16242. doi:10.1073/pnas.252582399

Livingstone CD, Barton GJ. 1993. Protein sequence alignments: a strategy for the hierarchical analysis of residue conservation. *Bioinformatics* **9**:745–756. doi:10.1093/bioinformatics/9.6.745

Long T, Qi X, Hassan A, Liang Q, De Brabander JK, Li X. 2020. Structural basis for itraconazole-mediated NPC1 inhibition. *Nat Commun* **11**:152. doi:10.1038/s41467-019-13917-5

Mahé Y, Lemoine Y, Kuchler K. 1996. The ATP Binding Cassette Transporters Pdr5 and Snq2 of Saccharomyces cerevisiae Can Mediate Transport of Steroids in Vivo*. *J Biol Chem* **271**:25167–25172. doi:10.1074/jbc.271.41.25167

Manolaridis I, Jackson SM, Taylor NMI, Kowal J, Stahlberg H, Locher KP. 2018. Cryo-EM structures of a human ABCG2 mutant trapped in ATP-bound and substrate-bound states. *Nature* **563**:426–430. doi:10.1038/s41586-018-0680-3

Meurs I, Lammers B, Zhao Y, Out R, Hildebrand RB, Hoekstra M, Van Berkel TJC, Van Eck M. 2012. The effect of ABCG1 deficiency on atherosclerotic lesion development in LDL receptor knockout mice depends on the stage of atherogenesis. *Atherosclerosis* **221**:41–47. doi:https://doi.org/10.1016/j.atherosclerosis.2011.11.024

Morin A, Eisenbraun B, Key J, Sanschagrin PC, Timony MA, Ottaviano M, Sliz P. 2013. Collaboration gets the most out of software. *Elife* **2**:e01456. doi:10.7554/eLife.01456

Nagy T, Tóth Á, Telbisz Á, Sarkadi B, Tordai H, Tordai A, Hegedűs T. 2021. The transport pathway in the ABCG2 protein and its regulation revealed by molecular dynamics simulations. *Cell Mol Life Sci* **78**:2329–2339. doi:10.1007/s00018-020-03651-3

Namba Y, Sogawa C, Okusha Y, Kawai H, Itagaki M, Ono K, Murakami J, Aoyama E, Ohyama K, Asaumi J, Takigawa M, Okamoto K, Calderwood SK, Kozaki K, Eguchi T. 2018.

Depletion of Lipid Efflux Pump ABCG1 Triggers the Intracellular Accumulation of Extracellular Vesicles and Reduces Aggregation and Tumorigenesis of Metastatic Cancer Cells . *Front Oncol* .

Nan W, Debin L, Wengen C, Fumihiko M, R. TA. 2004. ATP-binding cassette transporters G1 and G4 mediate cellular cholesterol efflux to high-density lipoproteins. *Proc Natl Acad Sci* **101**:9774–9779. doi:10.1073/pnas.0403506101

Orlando BJ, Liao M. 2020. ABCG2 transports anticancer drugs via a closed-to-open switch. *Nat Commun* **11**:2264. doi:10.1038/s41467-020-16155-2

Otwinowski Z, Minor WBT-M in E. 1997. [20] Processing of X-ray diffraction data collected in oscillation modeMacromolecular Crystallography Part A. Academic Press. pp. 307–326. doi:https://doi.org/10.1016/S0076-6879(97)76066-X

Pandzic E, Gelissen IC, Whan R, Barter PJ, Sviridov D, Gaus K, Rye K-A, Cochran BJ. 2017. The ATP binding cassette transporter, ABCG1, localizes to cortical actin filaments. *Sci Rep* **7**:42025. doi:10.1038/srep42025

Patel SB, Honda A, Salen G. 1998. Sitosterolemia: exclusion of genes involved in reduced cholesterol biosynthesis. *J Lipid Res* **39**:1055–1061. doi:10.1016/S0022-2275(20)33874-8

Pei J, Kim B-H, Grishin N V. 2008. PROMALS3D: a tool for multiple protein sequence and structure alignments. *Nucleic Acids Res* **36**:2295–2300. doi:10.1093/nar/gkn072

Pettersen EF, Goddard TD, Huang CC, Couch GS, Greenblatt DM, Meng EC, Ferrin TE. 2004. UCSF Chimera - A visualization system for exploratory research and analysis. *J Comput Chem* **25**:1605–1612. doi:10.1002/jcc.20084

Qi X, Schmiege P, Coutavas E, Wang J, Li X. 2018. Structures of human Patched and its complex with native palmitoylated sonic hedgehog. *Nature* **560**:128–132.

doi:10.1038/s41586-018-0308-7

Qian H, Zhao X, Cao P, Lei J, Yan N, Gong X. 2017. Structure of the Human Lipid Exporter ABCA1. *Cell* **169**:1228-1239.e10. doi:10.1016/j.cell.2017.05.020

Radhakrishnan A, Sun L-P, Kwon HJ, Brown MS, Goldstein JL. 2004. Direct Binding of Cholesterol to the Purified Membrane Region of SCAP: Mechanism for a Sterol-Sensing Domain. *Mol Cell* **15**:259–268. doi:10.1016/j.molcel.2004.06.019

Ristovski M, Farhat D, Bancud SEM, Lee J-Y. 2021. Lipid Transporters Beam Signals from Cell Membranes. *Membranes (Basel)* **11**:562. doi:10.3390/membranes11080562

Sag D, Cekic C, Wu R, Linden J, Hedrick CC. 2015. The cholesterol transporter ABCG1 links cholesterol homeostasis and tumour immunity. *Nat Commun* **6**:6354. doi:10.1038/ncomms7354

Sano O, Ito S, Kato R, Shimizu Y, Kobayashi A, Kimura Y, Kioka N, Hanada K, Ueda K, Matsuo M. 2014. ABCA1, ABCG1, and ABCG4 are distributed to distinct membrane meso-domains and disturb detergent-resistant domains on the plasma membrane. *PLoS One* **9**. doi:10.1371/journal.pone.0109886

Sano O, Kobayashi A, Nagao K, Kumagai K, Kioka N, Hanada K, Ueda K, Matsuo M. 2007. Sphingomyelin-dependence of cholesterol efflux mediated by ABCG1. *J Lipid Res* **48**:2377–2384. doi:10.1194/jlr.M700139-JLR200

Savary S, Denizot F, Luciani M-F, Mattei M-G, Chimini G. 1996. Molecular cloning of a mammalian ABC transporter homologous to Drosophila white gene. *Mamm Genome* **7**:673–676. doi:10.1007/s003359900203

Shapovalov M V, Dunbrack Jr RL. 2011. A smoothed backbone-dependent rotamer library for proteins derived from adaptive kernel density estimates and regressions. *Structure* **19**:844–

858. doi:10.1016/j.str.2011.03.019

Skarda L, Kowal J, Locher KP. 2021. Structure of the Human Cholesterol Transporter ABCG1. *J Mol Biol* **433**:167218. doi:https://doi.org/10.1016/j.jmb.2021.167218

Sun Y, Wang J, Long T, Qi X, Donnelly L, Elghobashi-Meinhardt N, Esparza L, Cohen JC, Xie X-S, Hobbs HH, Li X. 2021. Molecular basis of cholesterol efflux via ABCG subfamily transporters. *Proc Natl Acad Sci U S A* **118**:e2110483118. doi:10.1073/pnas.2110483118

Taylor NMI, Manolaridis I, Jackson SM, Kowal J, Stahlberg H, Locher KP. 2017. Structure of the human multidrug transporter ABCG2. *Nature* **546**:504–509. doi:10.1038/nature22345

Telbisz Á, Özvegy-Laczka C, Hegedűs T, Váradi A, Sarkadi B. 2013. Effects of the lipid environment, cholesterol and bile acids on the function of the purified and reconstituted human ABCG2 protein. *Biochem J* **450**:387–395. doi:10.1042/BJ20121485

Thompson JD, Higgins DG, Gibson TJ. 1994. CLUSTAL W: improving the sensitivity of progressive multiple sequence alignment through sequence weighting, position-specific gap penalties and weight matrix choice. *Nucleic Acids Res* **22**:4673–4680. doi:10.1093/nar/22.22.4673

Tian C, Huang D, Yu Y, Zhang J, Fang Q, Xie C. 2017. ABCG1 as a potential oncogene in lung cancer. *Exp Ther Med* **13**:3189–3194. doi:10.3892/etm.2017.4393

Vaughan AM, Oram JF. 2005. ABCG1 Redistributes Cell Cholesterol to Domains Removable by High Density Lipoprotein but Not by Lipid-depleted Apolipoproteins *. *J Biol Chem* **280**:30150–30157. doi:10.1074/jbc.M505368200

Wang J, Wang W, Kollman PA, Case DA. 2006. Automatic atom type and bond type perception in molecular mechanical calculations. *J Mol Graph Model* **25**:247–260. doi:https://doi.org/10.1016/j.jmgm.2005.12.005

Webb B, Sali A. 2014. Protein Structure Modeling with MODELLER BT - Protein Structure Prediction In: Kihara D, editor. New York, NY: Springer New York. pp. 1–15. doi:10.1007/978-1-4939-0366-5_1

Williams CJ, Headd JJ, Moriarty NW, Prisant MG, Videau LL, Deis LN, Verma V, Keedy DA, Hintze BJ, Chen VB, Jain S, Lewis SM, Arendall 3rd WB, Snoeyink J, Adams PD, Lovell SC, Richardson JS, Richardson DC. 2018. MolProbity: More and better reference data for improved all-atom structure validation. *Protein Sci* **27**:293–315. doi:10.1002/pro.3330

Xavier BM, Zein AA, Venes A, Wang J, Lee JY. 2020. Transmembrane polar relay drives the allosteric regulation for ABCG5/G8 sterol transporter. *Int J Mol Sci* **21**:1–20. doi:10.3390/ijms21228747

Xu D, Li Y, Yang F, Sun C-R, Pan J, Wang L, Chen Z-P, Fang S-C, Yao X, Hou W-T, Zhou C-Z, Chen Y. 2022. Structure and transport mechanism of the human cholesterol transporter ABCG1. *Cell Rep* **38**:110298. doi:https://doi.org/10.1016/j.celrep.2022.110298

Yang C, Yu L, Li W, Xu F, Cohen JC, Hobbs HH. 2004. Disruption of cholesterol homeostasis by plant sterols. *J Clin Invest* **114**:813–822. doi:10.1172/JCI22186

Yu L, Gupta S, Xu F, Liverman ADB, Moschetta A, Mangelsdorf DJ, Repa JJ, Hobbs HH, Cohen JC. 2005. Expression of ABCG5 and ABCG8 Is Required for Regulation of Biliary Cholesterol Secretion *. *J Biol Chem* **280**:8742–8747. doi:10.1074/jbc.M411080200

Yu L, von Bergmann K, Lutjohann D, Hobbs HH, Cohen JC. 2004. Selective sterol accumulation in ABCG5/ABCG8-deficient mice. *J Lipid Res* **45**:301–307. doi:10.1194/jlr.M300377-JLR200

Yu Q, Ni D, Kowal J, Manolaridis I, Jackson SM, Stahlberg H, Locher KP. 2021. Structures of ABCG2 under turnover conditions reveal a key step in the drug transport mechanism. *Nat*

Commun **12**:4376. doi:10.1038/s41467-021-24651-2

Zein AA, Kaur R, Hussein TOK, Graf GA, Lee J-Y. 2019. ABCG5/G8: a structural view to pathophysiology of the hepatobiliary cholesterol secretion. *Biochem Soc Trans* **47**:1259–1268. doi:10.1042/BST20190130

Zhang H, Huang C-S, Yu X, Lee J, Vaish A, Chen Q, Zhou M, Wang Z, Min X. 2021. Cryo-EM structure of ABCG5/G8 in complex with modulating antibodies. *Commun Biol* **4**:526. doi:10.1038/s42003-021-02039-8

Table 1: Crystallographic data collection and refinement.

Beamline	APS 19-ID
Number of crystals	3
Wavelength	0.9794
Resolution range	30.58 - 4.051 (4.195 - 4.051)*
Space group	I 2 2 2
Unit cell (*a, b, c* (Å))	173.268 230.11 249.819 90 90 90
Total reflections	427824 (30232)
Unique reflections	38173 (915)
Multiplicity	11.2 (14.4)
Completeness (%)	83.96 (22.75)
Mean I/sigma(I)	5.90 (1.41)
R-merge	3.392 (5.094)
CC1/2	0.377 (0.137)
CC*	0.74 (0.491)
Reflections used in refinement	34374 (915)
Reflections used for R-free	2016 (54)
R-work	0.2459 (0.2832)
R-free	0.3029 (0.3039)
CC(work)	0.864 (0.703)
CC(free)	0.817 (0.715)
Number of non-hydrogen atoms	18498

macromolecules	18442
ligands	56
RMS(bonds)	0.005
RMS(angles)	0.93
Ramachandran favored (%)	93.54
Ramachandran allowed (%)	5.90
Ramachandran outliers (%)	0.56
Rotamer outliers (%)	0.00
Clashscore	11.97
Average B-factor	52.45
macromolecules	52.45
ligands	49.48
Number of TLS groups	1

* Statistics for the highest-resolution shell are shown in parentheses.